

A HUBBLE SPACE TELESCOPE SURVEY OF H₂ EMISSION IN THE CIRCUMSTELLAR ENVIRONMENTS OF YOUNG STARS*

KEVIN FRANCE¹, ERIC SCHINDHELM^{1,9}, GREGORY J. HERCZEG^{2,10}, ALEXANDER BROWN¹, HERVÉ ABGRALL³, RICHARD D. ALEXANDER⁴, EDWIN A. BERGIN⁵, JOANNA M. BROWN⁶, JEFFREY L. LINSKY⁷, EVELYNE ROUEFF³, AND HAO YANG⁸

¹ Center for Astrophysics and Space Astronomy, University of Colorado, 389 UCB, Boulder, CO 80309, USA; kevin.france@colorado.edu

² Max-Planck-Institut für extraterrestrische Physik, Postfach 1312, D-85741 Garching, Germany

³ LUTH and UMR 8102 du CNRS, Observatoire de Paris, Section de Meudon, Place J. Janssen, F-92195 Meudon, France

⁴ Department of Physics and Astronomy, University of Leicester, Leicester LE1 7RH, UK

⁵ Department of Astronomy, University of Michigan, 830 Dennison Building, 500 Church Street, Ann Arbor, MI 48109, USA

⁶ Harvard-Smithsonian Center for Astrophysics, 60 Garden Street, MS-78, Cambridge, MA 02138, USA

⁷ JILA, University of Colorado and NIST, 440 UCB, Boulder, CO 80309, USA

⁸ Institute of Astrophysics, Central China Normal University, Wuhan, Hubei 430079, China

Received 2012 April 3; accepted 2012 July 17; published 2012 August 24

ABSTRACT

The formation timescale and final architecture of exoplanetary systems are closely related to the properties of the molecular disks from which they form. Observations of the spatial distribution and lifetime of the molecular gas at planet-forming radii ($a < 10$ AU) are important for understanding the formation and evolution of exoplanetary systems. Toward this end, we present the largest spectrally resolved survey of H₂ emission around low-mass pre-main-sequence stars compiled to date. We use a combination of new and archival far-ultraviolet spectra from the Cosmic Origins Spectrograph and Space Telescope Imaging Spectrograph instruments on the *Hubble Space Telescope* to sample 34 T Tauri stars (27 actively accreting Classical T Tauri Stars and 7 non-accreting Weak-lined T Tauri Stars) with ages ranging from ~ 1 to 10 Myr. We observe fluorescent H₂ emission, excited by Ly α photons, in 100% of the accreting sources, including all of the transitional disks in our sample (CS Cha, DM Tau, GM Aur, UX Tau A, LkCa 15, HD 135344B, and TW Hya). The spatial distribution of the emitting gas is inferred from spectrally resolved H₂ line profiles. Some of the emitting gas is produced in outflowing material, but the majority of H₂ emission appears to originate in a rotating disk. For the disk-dominated targets, the H₂ emission originates predominately at $a \lesssim 3$ AU. The emission line widths and inner molecular radii are found to be roughly consistent with those measured from mid-IR CO spectra.

Key words: protoplanetary disks – stars: pre-main sequence – ultraviolet: planetary systems

Online-only material: color figures, machine-readable table

1. INTRODUCTION

The lifetime, spatial distribution, and composition of gas and dust in the inner ~ 10 AU of young (age $\lesssim 10$ Myr) circumstellar disks are important components for understanding the formation and evolution of extrasolar planetary systems. The formation of giant planet cores and their accretion of gaseous envelopes occur on timescales similar to the lifetimes of the disks around Classical T Tauri Stars (CTTSs, 10^6 – 10^7 yr). The cores of giant planets are thought to be comprised of coagulations of dust grains (Hayashi et al. 1985), and the majority of observational work on the lifetime of inner disks has come from photometric and spectroscopic studies of their dust (Haisch et al. 2001; Hernández et al. 2007; Wyatt 2008). Dust in protoplanetary disks is observed as mid- and far-IR excess flux produced by warm grains (e.g., Furlan et al. 2006, 2009; Evans et al. 2009; Luhman et al. 2010). The IR spectral energy distributions (SEDs) of protoplanetary disks are sensitive to the radial distribution of dust in the disk; this dependence has led to the discovery

of a class of “transitional” systems, whose SEDs indicate that gaps of a few tenths to tens of AU have been opened in their inner disks (Strom et al. 1989; Calvet et al. 2002, 2005; Espaillat et al. 2007a; and see the review by Williams & Cieza 2011). The physical process by which the inner disk is cleared is not yet established. Possible mechanisms including photoevaporation (Alexander et al. 2006; Gorti et al. 2009) and dynamical clearing by exoplanetary systems (Rice et al. 2003; Dodson-Robinson & Salyk 2011), possibly aided by the magnetorotational instability (Chiang & Murray-Clay 2007), can reproduce certain transitional disk observations.

The lifetime and spatial extent of the gas disk determine the final mass of giant planets (Ida & Lin 2004) and the final architecture of an exoplanetary system, as disk gas regulates type-II planetary migration (Ward 1997; Armitage et al. 2002; Trilling et al. 2002). Because the migration timescale is sensitive to the specifics of the disk surface density distribution and dissipation timescale (Armitage 2007), observations of gas-rich systems with age ≤ 10 Myr can provide important constraints on models of the evolution of exoplanetary systems. Significant observational effort has been devoted to the study of inner disk gas in recent years, including ground-based mid-IR spectroscopy of CO and [Ne II] (Najita et al. 2003, 2009; Pascucci et al. 2007; Herczeg et al. 2007; Bast et al. 2011; Sacco et al. 2012), spectroastrometric observations of CO (Pontoppidan et al. 2008, 2011) and [Ne II] (Pascucci et al. 2011), and *Spitzer* Infrared Spectrograph (IRS) observations of H₂O and organics (Carr &

* Based on observations made with the NASA/ESA *Hubble Space Telescope*, obtained from the data archive at the Space Telescope Science Institute. STScI is operated by the Association of Universities for Research in Astronomy, Inc. under NASA contract NAS 5-26555.

⁹ Current address: Southwest Research Institute, 1050 Walnut Street, Suite 300, Boulder, CO 80302, USA.

¹⁰ Current address: Kavli Institute for Astronomy and Astrophysics, Peking University, Beijing 100871, China.

Najita 2008, 2011; Salyk et al. 2008, 2011b). There is growing evidence that remnant gas disk survival is common inside the dust hole in transitional disks (e.g., Salyk et al. 2009, 2011a), suggesting that planetary migration may continue after the dust disk has dispersed. In transitional systems with minimal inner disk dust, observations of active accretion also provide indirect evidence for the presence of a remnant gas disk (Najita et al. 2007; Kim et al. 2009; Merín et al. 2010; Fedele et al. 2010).

Many previous studies of inner disk gas have used trace species to infer the presence of molecular hydrogen (H_2), the primary constituent of protoplanetary disks and gas giant planets. The homonuclear nature of H_2 means that rovibrational transitions are dipole forbidden, with weak quadrupole transitions that have large energy spacings. This makes direct detection of H_2 challenging at near- and mid-IR wavelengths (Pascucci et al. 2006; Carmona et al. 2008; but see also Bary et al. 2008). However, H_2 can be observed in the far-UV (912–1650 Å) bandpass, where the strong dipole-allowed electronic transition spectrum is primarily photoexcited (“pumped”) by stellar $Ly\alpha$ photons (Ardila et al. 2002; Herczeg et al. 2002). The $Ly\alpha$ -pumping route proceeds primarily by absorption out of the second excited vibrational level ($v = 2$) of H_2 (Shull 1978), which implies that the molecules reside in a hot ($T(H_2) > 2000$ K) disk surface at semi-major axes $a < 10$ AU (Herczeg et al. 2004), or in extended outflows (Walter et al. 2003; Saucedo et al. 2003). An analysis of the spectral line profiles can distinguish between these origins, enabling one to identify and characterize emission from the molecular disk given sufficient spectral resolution and spectroscopic sensitivity. Assuming that disk molecules are in Keplerian orbit around their central star, line broadening due to orbital motion dominates the profile in moderate-to-high inclination systems. H_2 velocity widths can therefore be used to infer the spatial distribution of the gas on the disk surface.

In this work, we present the most sensitive survey of spectrally resolved H_2 emission in protoplanetary disks obtained to date. Previous spectral surveys of T Tauri Stars (TTs) with the *International Ultraviolet Explorer* (Valenti et al. 2000; Johns-Krull et al. 2000) and the various ultraviolet spectrographs on *Hubble Space Telescope* (*HST*; Ardila et al. 2002; Herczeg et al. 2006; Ingleby et al. 2009; Yang et al. 2012) have been carried out at either lower spectroscopic sensitivity or resolution. In this study, we take advantage of the high sensitivity, low instrumental background, and moderate spectral resolution of the *HST*-Cosmic Origins Spectrograph (COS) to greatly expand the number of targets available for detailed UV studies. In Section 2, we describe the targets and the *HST* observations. The analysis performed to characterize the H_2 luminosities and spatial distributions is described in Section 3. We present in Section 4 a discussion of H_2 line profiles, considering outflow and disk origins for the emitting gas, and an estimate of the fraction of stellar $Ly\alpha$ reprocessed by circumstellar H_2 . Section 4 also presents the time evolution of the amount and location of the H_2 gas, suggesting that the H_2 -emitting gas both dissipates and moves toward larger orbital radii over the interval from 10^6 to 10^7 yr. A brief summary of the results from the molecular survey is presented in Section 5.

2. TARGET SAMPLE AND OBSERVATIONS

2.1. Target Sample

The goal of this observational survey is to span a range of ages, mass accretion rates, and star-forming environments in order to better understand the global properties of H_2 emis-

sion in protoplanetary environments. The targets mainly belong to the Taurus–Auriga, η Chamaeleontis, TW Hya, and Chamaeleon I star-forming regions, as well as individual targets in other associations and isolated systems. Potential sources of uncertainty in analyzing a diverse population of targets are systematic effects based on different methods used to derive system parameters in the literature. In order to mitigate the effects of systematics on this study of molecular disks, our approach was to adopt system parameters from papers where similar techniques were used to derive properties such as ages, extinctions, stellar masses, and inclinations. The target parameters adopted are given in Table 1. Where possible, (1) inclinations were taken from submillimeter/IR interferometric studies; (2) ages, stellar masses, and extinctions were derived from pre-main-sequence stellar evolutionary tracks; and (3) mass accretion rates were derived from measurements of the accretion luminosity. Of our 34 targets, 27 are considered CTTSs while 7 do not show evidence for active accretion or a gas-rich circumstellar disk and are classified as Weak-lined T Tauri Stars (WTTSs). These populations are separated as the upper and lower groups, respectively, of target stars listed in Table 1. Seven of the CTTSs in our sample are considered transitional systems (CS Cha, DM Tau, GM Aur, UX Tau A, LkCa 15, HD 135344B, and TW Hya), with mid-IR SEDs indicating that a gap has opened in their inner dust disks. This sample includes several of the best-studied transitional disks in the literature. References are listed in Table 1, and a more detailed description of a subsample of these targets can be found in Schindhelm et al. (2012a).

The assumed distances are not critical to the results presented here, but they do impact the comparison of the H_2 , $Ly\alpha$, and C IV luminosities presented in Section 4. For the Taurus–Auriga targets (AA Tau, BP Tau, DE Tau, DF Tau, DK Tau, DM Tau, DN Tau, DR Tau, GM Aur, HN Tau, IP Tau, LkCa 15, RW Aur, SU Aur, UX Tau A, V836 Tau, HBC 427 (V397 Tau), LkCa 19, LkCa 4), we assumed $d = 140$ pc (Elias 1978; Kenyon & Hartmann 1995; and see also the Very Long Baseline Array work presented by Loinard et al. 2007); for the η Cha targets (RECX 11, RECX 15, RECX 1), we assumed $d = 97$ pc (Mamajek et al. 1999); for the TW Hya association targets (TW Hya, TWA 13A, TWA 13B, TWA 7), we assumed $d = 54$ pc (van Leeuwen 2007), and for Chamaeleon I (CS Cha, CV Cha), we assumed $d = 160$ pc (Luhman 2004). Other objects are V4046 Sgr ($d = 83$ pc; Quast et al. 2000), SZ 102 (in Lupus 3, $d = 200$ pc; Comerón et al. 2003), HD 104237 (a member of the ϵ Cha group, $d = 116$ pc; Feigelson et al. 2003), AK Sco ($d = 103$ pc; van Leeuwen 2007), and RU Lupi ($d = 121$ pc; van Leeuwen 2007). Six of the nineteen sources in Taurus–Auriga are known multi-star systems (see, e.g., Kraus et al. 2012) and V4046 Sgr is known to be a short-period binary system (Quast et al. 2000).

2.2. Observations

Our sample of 34 TTs was assembled from new and archival observations with *HST*-COS and -STIS. The majority of the targets were observed as part of the DAO of Tau guest observing program (PID 11616; PI: G. Herczeg) and the COS Guaranteed Time Observing program (PIDs 11533 and 12036; PI: J. Green). Additional observations of the transitional disk HD 135344B and weak-lined systems TWA 13A and TWA 13B (PIDs 11828 and 12361; PI: A. Brown) are presented. A subset of the H_2 survey observations have been presented previously in the literature (France et al. 2011a, 2011b, 2012; Ingleby

Table 1
HST Target List

Target ^a	A_V	$\log_{10}(\text{Age})$ (yr)	M_* (M_\odot)	\dot{M} ($10^{-8} M_\odot \text{ yr}^{-1}$)	i ($^\circ$)	<i>HST</i> ^b PID	Ref. ^c
AA Tau	0.50	6.38 ± 0.20	0.80	0.33	75	11616	2,15,28
AK Sco	0.5	7.24 ± 0.24	1.35	0.09	68	11616–S	3,24
BP Tau	0.50	5.94 ± 0.29	0.73	2.88	30	12036	1,15,30
CS Cha	0.8	6.39 ± 0.09	1.05	1.20	60	11616	4,25
CV Cha	1.67	6.70 ± 0.10	2.00	3.16	35	11616–S	5,26
DE Tau	0.60	5.82 ± 0.20	0.59	2.64	35	11616	1,15,29
DF Tau A	0.60	6.27 ± 0.53	0.19	17.7	85	11533	15,29
DK Tau A	0.80	6.17 ± 0.22	0.71	3.79	50	11616	1,15,29
DM Tau	0.0	6.56 ± 0.20	0.50	0.29	35	11616	2,16,21
DN Tau	1.90	6.04 ± 0.20	0.60	0.35	28	11616	2,15,21,31
DR Tau	3.20	6.18 ± 0.20	0.80	3.16	72	11616	2,17,28
GM Aur	0.10	6.86 ± 0.20	1.20	0.96	55	11616	2,15,21
HD 104237	0.70	6.30 ± 0.30	2.50	3.50	18	11616–S	7,19,40
HD 135344B	0.30	6.90 ± 0.30	1.60	0.54	14	11828	8,19,36
HN Tau A	0.5	6.27 ± 0.27	0.85	0.13	>40	11616	1,15,22
IP Tau	0.20	6.37 ± 0.24	0.68	0.08	60	11616	1,15,32
LkCa 15	0.60	6.35 ± 0.26	0.85	0.13	49	11616	1,16,21
RECX 11	0.0	6.60 ± 0.20	0.80	0.03	70	11616	9,20,45
RECX 15	0.0	6.78 ± 0.08	0.40	0.10	60	11616	10,20
RU Lupi	0.07	6.39 ± 0.09	0.80	3.00	24	12036	11,18,34
RW Aur A	1.6	5.85 ± 0.53	1.40	3.16	77	11616	1,23,35
SU Aur	0.9	6.39 ± 0.21	2.30	0.45	62	11616	1,17,37
SZ 102	1.13	6.15 ± 0.15	0.75	0.08	10	11616	12,27,38
TW Hya	0.0	7.00 ± 0.40	0.60	0.02	4	8041–S	13,18,36
UX Tau A	0.20	6.10 ± 0.30	1.30	1.00	35	11616	1,21
V4046 Sgr	0.0	6.90 ± 0.12	0.86+0.69	1.30	36	11533	14,22,39
V836 Tau	1.70	6.26 ± 0.26	0.75	0.01	65	11616	1,18,41
HBC 427	0.00	6.64 ± 0.14	0.7	11616	6
LkCa 19	0.00	6.84 ± 0.38	1.35	11616	1
LkCa 4	0.69	6.43 ± 0.25	0.77	11616	6
RECX 1	0.00	6.78 ± 0.00	0.90	11616	42
TWA 13A	0.00	6.90 ± 0.12	0.32	12361	43
TWA 13B	0.00	6.90 ± 0.12	0.38	12361	43
TWA 7	0.00	6.39 ± 0.39	0.55	11616	44

Notes.

^a Targets in the upper group are CTTs, targets in the lower group are WTTSs.

^b Program IDs marked –S indicate that STIS observations were used.

^c (1) Kraus & Hillenbrand 2009; (2) Ricci et al. 2010, age uncertainties are assumed to be ± 0.20 ; (3) Alencar et al. 2003; (4) Lawson et al. 1996; (5) Siess et al. 2000; (6) Bertout et al. 2007; (7) Feigelson et al. 2003; (8) van Boekel et al. 2005; (9) Lawson et al. 2001; (10) Ramsay Howat & Greaves 2007; (11) Herczeg et al. 2005; (12) Comerón & Fernández 2010; (13) Webb et al. 1999; (14) Quast et al. 2000; (15) Gullbring et al. 1998; (16) Hartmann et al. 1998; (17) Gullbring et al. 2000; (18) Herczeg & Hillenbrand 2008; (19) Garcia Lopez et al. 2006; (20) Lawson et al. 2004; (21) Andrews et al. 2011; (22) France et al. 2011b; (23) White & Ghez 2001; (24) Gómez de Castro 2009; (25) Espaillat et al. 2007a; (26) Hussain et al. 2009; (27) Comerón et al. 2003; (28) Andrews & Williams 2007; (29) Johns-Krull & Valenti 2001; (30) Simon et al. 2000; (31) Muzerolle et al. 2003; (32) Espaillat et al. 2010; (34) Stempels et al. 2007; (35) Eisner et al. 2007; (36) Pontoppidan et al. 2008; (37) Akeson et al. 2002; (38) Coffey et al. 2004; (39) Rodríguez et al. 2010; (40) Grady et al. 2004; (41) Najita et al. 2008; (42) Ingleby et al. 2011b; (43) Plavchan et al. 2009; (44) Neuhäuser et al. 2000; (45) Ingleby et al. 2011a.

et al. 2011b; Yang et al. 2011; Schindhelm et al. 2012a). Finally, we have included archival Space Telescope Imaging Spectrograph (STIS) observations of the well-studied CTTS TW Hya (Herczeg et al. 2002), obtained through StarCAT (Ayes 2010).

Most of the targets were observed with the medium-resolution far-UV modes of COS (G130M and G160M; Green et al. 2012). These observations were acquired between 2009 December and 2011 September. Multiple central wavelength settings at several focal-plane split positions were used to create continuous far-UV spectra from ≈ 1150 to 1750 \AA and mitigate the effects of fixed pattern noise. These modes provide a point-source resolution of $\Delta v \approx 17 \text{ km s}^{-1}$ with 7 pixels per resolution

element (Osterman et al. 2011). The data were smoothed by 3 pixels for analysis. The total far-UV exposure times were between two and four orbits per target, depending on the intrinsic luminosity and the interstellar plus circumstellar reddening on the sightline. The one-dimensional spectra produced by the COS calibration pipeline, CALCOS, were aligned and co-added using the custom software procedure described by Danforth et al. (2010). The full far-UV spectra of three CTTs (AA Tau, V4046 Sgr, and GM Aur) and one WTTS (LkCa 19) are displayed in Figure 1, and a 40 \AA blow-up of the CTTs is shown in Figure 2.

Targets that exceeded the COS bright-object limit were observed with STIS in the medium-resolution echelle mode. We used the E140M mode ($\Delta v \approx 8 \text{ km s}^{-1}$) mode through

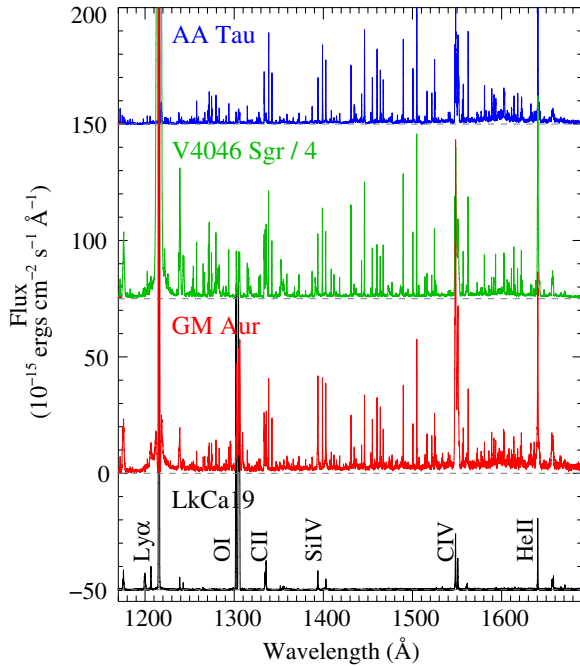


Figure 1. Examples of COS spectra (1170–1690 Å) for a range of gas and dust parameters. From top to bottom: the primordial disk target AA Tau (offset by $+150 (\times 10^{-15} \text{ erg cm}^{-2} \text{ s}^{-1} \text{ Å}^{-1})$), the pre-transitional disk V4046 Sgr (flux divided by 4 and offset by $+75 (\times 10^{-15} \text{ erg cm}^{-2} \text{ s}^{-1} \text{ Å}^{-1})$), the transitional disk system GM Aur, and the gas-poor WTTS LkCa 19 (offset by $-50 (\times 10^{-15} \text{ erg cm}^{-2} \text{ s}^{-1} \text{ Å}^{-1})$). The spectra have been binned by one spectral resolution element (7 pixels) for display. Except for the atomic lines identified in the spectrum of LkCa 19, most of the emission lines in the spectra of the other three stars are fluorescent H_2 emission lines pumped by $\text{Ly}\alpha$.

(A color version of this figure is available in the online journal.)

the $0'.2 \times 0'.2$ slit for exposure times between two and three orbits per object. The far-UV STIS spectra were combined using the STIS echelle software developed for the StarCAT catalog (Ayres 2010, T. Ayres 2011, private communication).

3. ANALYSIS

We observe fluorescent H_2 emission from all of the 27 CTTSs in our sample, and no H_2 emission from the 7 WTTS targets. The number of observed fluorescent progressions varies significantly across the sample, and we present our measurements of the total H_2 fluxes below. We detect strong fluorescent emission in all of the transitional objects in our sample (CS Cha, DM Tau, GM Aur, UX Tau A, LkCa 15, HD 135344B, and TW Hya; Section 4.3).

The fluorescent H_2 lines observed in the CTTS sample can be used to determine the relative amount of H_2 in the circumstellar environment and to constrain its spatial distribution. For our line-profile analysis, we focus on the measurement of two progressions ($[v', J'] = [1, 7]$ and $[1, 4]$) detected in all of the CTTS targets.¹¹ These emission lines are pumped through the $(1-2)\text{R}(6)$ $\lambda_{\text{lab}} 1215.73 \text{ Å}$ and $(1-2)\text{P}(5)$ $\lambda_{\text{lab}} 1216.07 \text{ Å}$ transitions, respectively. The absorbing transitions are within $+15$ to $+100 \text{ km s}^{-1}$ of $\text{Ly}\alpha$ line center. The signal-to-noise

¹¹ The quantum numbers v and J denote the vibrational and rotational quantum numbers in the ground electronic state ($X^1\Sigma_g^+$), the numbers v' and J' characterize the H_2 in the excited ($B^1\Sigma_u^+$) electronic state, and the numbers v'' and J'' are the rovibrational levels in the electronic ground state following the fluorescent emission. Absorption lines are described by $(v' - v)$ and emission lines by $(v' - v'')$.

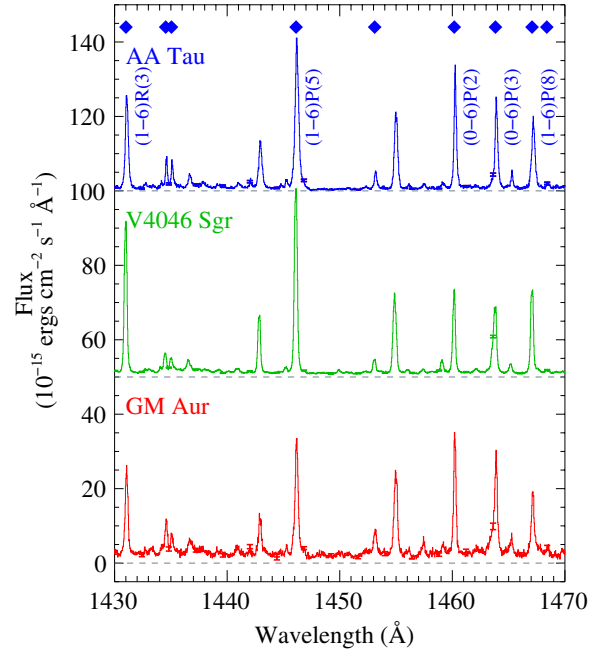


Figure 2. The 1430–1470 Å spectral region for the gas-rich targets plotted in Figure 1. All of the strong spectral features in this bandpass are emission lines from $\text{Ly}\alpha$ -pumped fluorescent H_2 . Emission lines used in this analysis are marked with blue diamonds and several bright features are labeled. Objects are plotted in order of decreasing near-IR dust excesses: AA Tau (primordial, $n_{13-31} = -0.51$; Furlan et al. 2009), V4046 Sgr (pre-transitional) has a sub-AU scale hole in the inner disk dust distribution (Jensen & Mathieu 1997), and GM Aur (transitional, $n_{13-31} = 1.75$; Furlan et al. 2009) has an $\sim 24 \text{ AU}$ hole in the inner dust disk (Calvet et al. 2005). The spectra are binned to $\approx 1/2$ of a spectral resolution element (3 pixels), and representative error bars are shown overplotted. The H_2 spectra are qualitatively similar, independent of the inner disk dust properties.

(A color version of this figure is available in the online journal.)

ratios (S/N) per resolution element are typically between 5 and 40 in the brightest fluorescent H_2 emission lines for our CTTS targets. The $(1-7)\text{R}(3)$ $\lambda_{\text{lab}} = 1489.57 \text{ Å}$ transition is relatively free from spectral contamination and is displayed for all targets in Figures 3(a)–(c). When available, the stellar radial velocities are indicated in Figure 3 with green dash-dotted lines. Within the $\sim 15 \text{ km s}^{-1}$ wavelength solution accuracy of COS, most of the H_2 progressions are consistent with the stellar velocity. In several cases the H_2 lines appear to have line wings extending to negative velocities or statistically significant differences in the velocity widths of different H_2 progressions. RW Aur is an extreme example of this behavior. Ardila et al. (2002) and Herczeg et al. (2006) have noted the presence of blueshifted H_2 emission in their sample of TTSs observed with GHRS and STIS. The presence of blueshifted emission creates additional uncertainty in the measured line widths at the resolution of our spectra, and we present a discussion of outflow signatures observed in our sample in Section 4.2.1.

The high S/N of the COS data means that we can restrict the analysis to the brightest lines from the progressions of interest. Systematics were minimized by focusing on emission lines with wavelengths $1395 \lesssim \lambda \lesssim 1640 \text{ Å}$. This choice is optimal because (1) fluorescent transitions cascading to vibrational levels $v'' \gtrsim 5$ do not suffer significant self-absorption before escaping the circumstellar environment (e.g., Figure 7 of Herczeg et al. 2004), enabling more robust flux measurements; (2) the non-Gaussian wings of the COS instrumental line-spread function

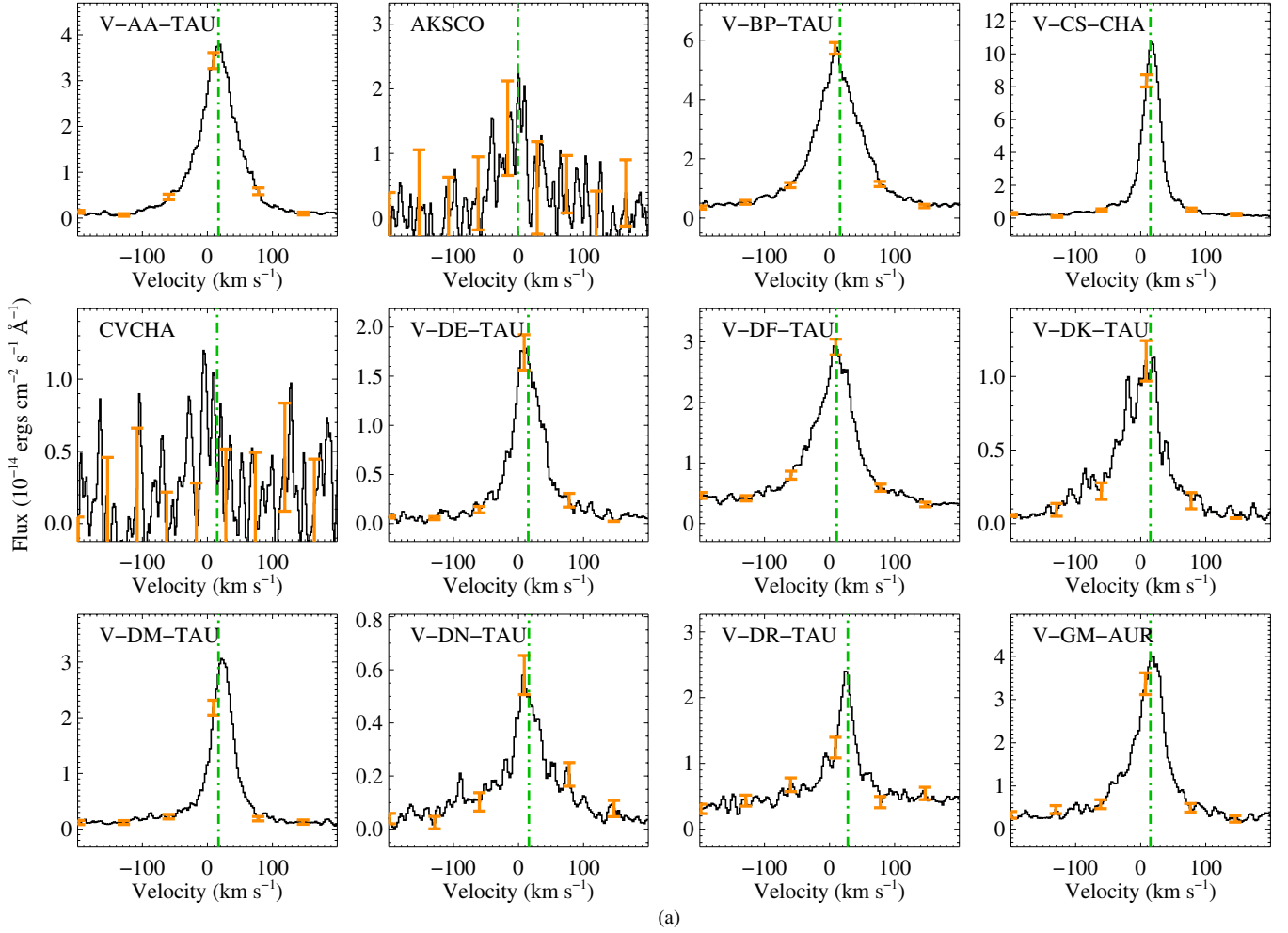


Figure 3. Velocity profiles for the $\text{H}_2 B^1\Sigma_u^+ - X^1\Sigma_g^+ (1-7) R(3)$ ($\lambda_{\text{lab}} = 1489.57 \text{ \AA}$) emission line in all targets, plotted over the $\pm 200 \text{ km s}^{-1}$ interval. The data plotted here are smoothed to 3 pixels (≈ 0.5 spectral resolution elements), with representative error bars shown in orange. The green dash-dotted line is plotted at the stellar radial velocity, when known. The target labels are the target names identified in the headers of the *HST* spectroscopic observations.

(A color version of this figure is available in the online journal.)

(LSF¹²) contain a smaller fraction of the power at $\lambda > 1400 \text{ \AA}$; (3) the strongest lines from the [1,4] and [1,7] progressions are in this range; and (4) the relative correction for interstellar reddening between the different fluorescent emission lines is minimized. The first and latter two arguments apply equally to the STIS data.

3.1. Line Fluxes and the H_2 Progression Luminosity

The H_2 emission lines were fitted with an interactive multi-Gaussian IDL line-fitting code optimized for COS emission line spectra. This code assumes a Gaussian line shape convolved with the wavelength-dependent LSF, then uses the MPFIT routine to minimize χ^2 between the fit and data (Markwardt 2009). A second-order polynomial background, the Gaussian amplitudes, and the Gaussian FWHMs for each component are free parameters. The parameters of the underlying Gaussian emission lines are returned to the user. The smaller STIS aperture does not sample the broad wings of the *HST* LSF; therefore unconvolved Gaussians were used for the targets observed with STIS. We chose 12 progressions with absorbing transitions that

spanned the width of the observed Ly α profiles in most targets, $1213.3 \leq \lambda_{\text{abs}}(\text{H}_2) \leq 1219.1 \text{ \AA}$ (Schindhelm et al. 2012b). We fitted the brightest unblended lines from 12 progressions in the 1395–1640 \AA bandpass, and used these values to determine the total flux from each progression.

A list of the selected lines is given in Table 2. The total flux from a given progression is given by

$$F_m(\text{H}_2) = \frac{1}{N} \sum \left(\frac{F_{mn}}{B_{mn}} \right), \quad (1)$$

where F_{mn} is the reddening-corrected, integrated H_2 emission line flux from rovibrational state m ($= [v', J']$) in the $B^1\Sigma_u^+$ electronic state to n ($= [v'', J'']$) in the ground electronic state, $X^1\Sigma_g^+$. B_{mn} is the branching ratio between these two states, and N is the number of emission lines measured from a given progression. The measurement errors are typically small, so we take the flux error to be the standard deviation of the individual measurements of $F_m(\text{H}_2)$. The dominant systematic error on the measured H_2 flux is the correction for interstellar reddening; we do not attempt to account for this uncertainty in the flux and luminosity errors presented below. In Table 3, we present reddening-corrected progression fluxes (in units of $10^{-14} \text{ erg cm}^{-2} \text{ s}^{-1}$) for all of the gas-rich targets. The total progression luminosity is then $L_m(\text{H}_2) = (4\pi d^2)F_m(\text{H}_2)$. Upper

¹² The LSF experiences a wavelength-dependent non-Gaussianity due to the introduction of mid-frequency wave-front errors produced by the polishing errors on the *HST* primary and secondary mirrors; <http://www.stsci.edu/hst/cos/documents/isrs/>

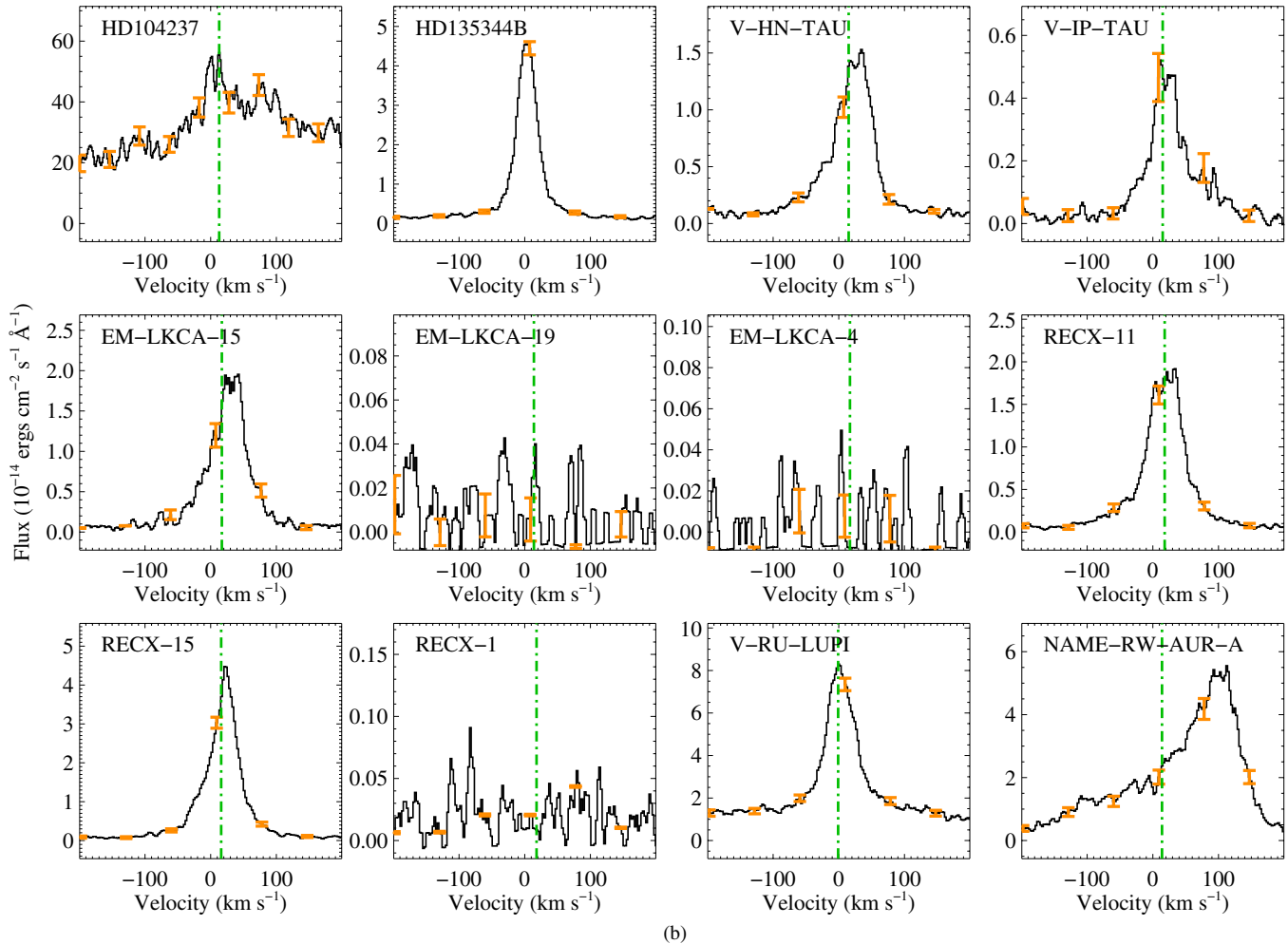


Figure 3. (Continued)

limits on the H_2 emission line fluxes in the gas-depleted targets were determined from the standard deviation in a $\pm 50 \text{ km s}^{-1}$ region surrounding the laboratory wavelength of the transition. The total fluorescent H_2 luminosity is then taken as the sum of all 12 of the fluorescent progressions. This prescription should account for $\gtrsim 80\%$ of the total $\text{Ly}\alpha$ -pumped H_2 emission from our targets, although the exact fraction of the total measured H_2 flux will depend on the local $\text{Ly}\alpha$ line profile (Herczeg et al. 2004; Schindhelm et al. 2012b).

Depending on the geometry and spatial distribution of the absorbing molecular layer, the H_2 absorption lines may be optically thin (or have optical depths of a few) in some targets. In this case, the emitted H_2 luminosity will be directly proportional to the number of $\text{Ly}\alpha$ -pumping photons received. Schindhelm et al. (2012b) have presented total incident $\text{Ly}\alpha$ fluxes for 14 of the targets in our sample. Using a line-profile reconstruction technique that takes into account the 12 H_2 progressions described above, they simultaneously fit the neutral hydrogen outflow, the H_2 column density, and the H_2 temperature (previous examples of H_2 -based $\text{Ly}\alpha$ reconstructions are described by Wood et al. 2002; Wood & Karvoska 2004; Herczeg et al. 2004). The amount of the stellar $\text{Ly}\alpha$ that is redistributed by H_2 can be determined by dividing the total H_2 flux, $F(H_2)$, by the total $\text{Ly}\alpha$ flux, $F(H_2)/F(\text{Ly}\alpha)$. The H_2 luminosity can also be compared to accretion indicators in our data set, such as C IV. Emission from the C IV $\lambda\lambda 1548, 1550$ resonance doublet in excess of a baseline magnetospheric level has been shown to correlate with the mass

accretion rate (Johns-Krull et al. 2000; Yang et al. 2012). The C IV flux can be measured directly in the same data set from which we measure $F_m(H_2)$, mitigating complications associated with short- and long-baseline time variability. Due to the non-Gaussian appearance of many of the C IV emission profiles, we measured $F(C\text{ IV})$ by integrating the reddening-corrected spectra over (1547.5–1553.5 Å) and subtracted the continuum from an adjacent, line-free portion of the spectrum.

3.2. H_2 Line Widths and the Average H_2 Radius, $\langle R_{H_2} \rangle$

Figure 4 shows the H_2 (1–6)P(5) ($\lambda_{\text{lab}} = 1446.12 \text{ \AA}$) profiles of the three example spectra displayed in Figure 2, with the 1450 \AA *HST*+COS LSF overplotted as the gray dash-dot line. These spectra are typical of the CTTS sample and one observes that the emission lines are spectrally resolved. We display the basic H_2 and C IV line parameter observations for the [1,7] and [1,4] progressions in Figure 5. The H_2 emission line FWHMs are uncorrelated with the stellar mass, $F_m(H_2)$, or $F(C\text{ IV})$.

Kinematic broadening dominates the observed H_2 line profiles (see Section 4.2). The thermal broadening of the emission lines is approximately 4.5 km s^{-1} at the nominal 2500 K H_2 layer; significant additional broadening would require temperatures in excess of the $\approx 4500 \text{ K}$ dissociation temperature of H_2 (Lepp & Shull 1983). If we further assume that any turbulence in the disks is subsonic, then the maximum turbulent velocity will be no larger than a few km s^{-1} . Therefore, velocity

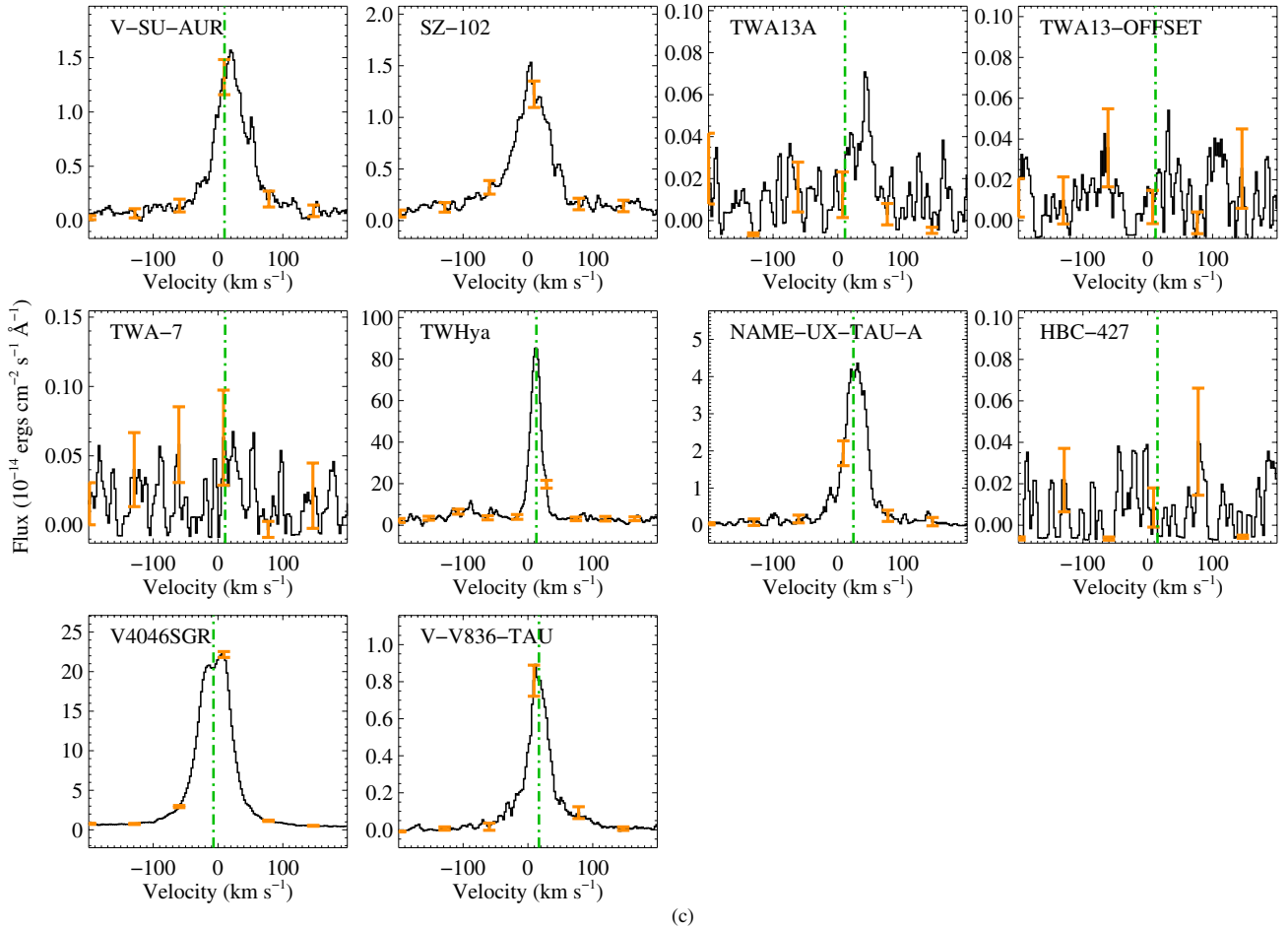


Figure 3. (Continued)

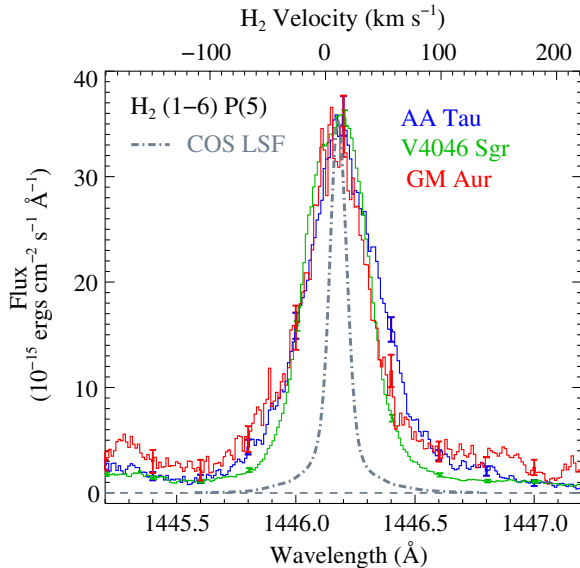


Figure 4. Expanded view of the H_2 (1–6) P(5) ($\lambda_{\text{lab}} = 1446.12 \text{ \AA}$) emission line, showing the velocity width beyond the COS line-spread function (shown as the gray dash-dotted line) for the three example targets shown in Figure 2. The AA Tau and V4046 Sgr spectra have been normalized to the peak flux of the GM Aur H_2 emission and shifted to the centroid velocity of the H_2 emission. The emission lines are spectrally resolved by COS.

(A color version of this figure is available in the online journal.)

broadening due to bulk motions and Keplerian rotation dominate the observed line shapes when the FWHM of the emission line is greater than the 17 km s^{-1} spectral resolution of COS. For the case of H_2 in a circumstellar disk, we define a simple metric to characterize the average H_2 radius, $\langle R_{\text{H}_2} \rangle$,

$$\langle R_{\text{H}_2} \rangle_m = GM_* \left(\frac{2 \sin(i)}{\text{FWHM}_m} \right)^2, \quad (2)$$

where M_* is the stellar mass, i is the inclination angle, and FWHM_m is the mean of the Gaussian FWHMs for a given progression m . This definition of the average molecular radius is analogous to the UV-CO radius used by Schindhelm et al. (2012a). When possible, we use disk inclinations derived from the submillimeter dust continuum observations presented by Andrews & Williams (2007) and Andrews et al. (2011). In principle, the error on the average H_2 radius should include uncertainties on the stellar mass and disk inclinations; however these uncertainties are not available for all targets. Therefore, the quoted error on $\langle R_{\text{H}_2} \rangle$ only includes measurement uncertainties from the H_2 line fitting.

In Table 4 we present $\langle R_{\text{H}_2} \rangle$ for the $[v', J'] = [1, 7]$ progression ($\equiv \langle R_{\text{H}_2} \rangle_{[1,7]}$). We focus on the $[1, 7]$ progression due to its proximity to the $\text{Ly}\alpha$ line center. This progression should be one of the most readily observable in weakly accreting systems because as the accretion-powered $\text{Ly}\alpha$ flux decreases, the flux in the wings of $\text{Ly}\alpha$ may be insufficient to excite a detectable level of H_2 emission. However, the $[1, 7]$ progression should continue to be observable even in systems with narrow $\text{Ly}\alpha$ profiles (e.g.,

Table 2
Selected H₂ Emission Lines

Line ID ^a	[<i>v</i> ', <i>J</i> ']	λ _{lab} (Å)	<i>B_{mn}</i> ^b	λ _{pump} (Å)
(3–9)P(14)	[3,13]	1608.33	0.139	1213.36
(3–10)R(12)	[3,13]	1615.43	0.125	1213.36
(4–6)R(12)	[4,13]	1415.33	0.037	1213.68
(4–8)R(12)	[4,13]	1509.45	0.023	1213.68
(4–11)R(12)	[4,13]	1613.99	0.092	1213.68
(3–5)R(15)	[3,16]	1418.23	0.050	1214.47
(3–7)R(15)	[3,16]	1513.99	0.057	1214.47
(3–9)R(15)	[3,16]	1593.26	0.122	1214.47
(3–10)R(15)	[3,16]	1621.12	0.062	1214.47
(4–8)P(5)	[4,4]	1477.05	0.039	1214.78
(4–9)P(5)	[4,4]	1526.55	0.033	1214.78
(4–11)P(5)	[4,4]	1613.72	0.150	1214.78
(1–6)P(8)	[1,7]	1467.08	0.080	1215.73
(1–7)R(6)	[1,7]	1500.45	0.101	1215.73
(1–7)P(8)	[1,7]	1524.65	0.111	1215.73
(1–8)R(6)	[1,7]	1556.87	0.074	1215.73
(1–6)R(3)	[1,4]	1431.01	0.058	1216.07
(1–6)P(5)	[1,4]	1446.12	0.083	1216.07
(1–7)R(3)	[1,4]	1489.57	0.094	1216.07
(1–7)P(5)	[1,4]	1504.76	0.115	1216.07
(3–7)P(1)	[3,0]	1435.05	0.118	1217.04
(3–10)P(1)	[3,0]	1591.32	0.233	1217.04
(3–11)P(1)	[3,0]	1636.34	0.099	1217.04
(0–5)P(2)	[0,1]	1398.95	0.141	1217.21
(0–6)P(2)	[0,1]	1460.17	0.083	1217.21
(0–2)P(2)	[0,1]	1521.59	0.032	1217.21
(0–5)P(3)	[0,2]	1402.65 ^c	0.126	1217.64
(0–6)P(3)	[0,2]	1463.83	0.074	1217.64
(0–7)P(3)	[0,2]	1525.15	0.029	1217.64
(2–5)P(13)	[2,12]	1434.54	0.066	1217.90
(2–6)R(11)	[2,12]	1453.10	0.049	1217.90
(2–8)R(11)	[2,12]	1555.89	0.077	1217.90
(2–8)P(13)	[2,12]	1588.80	0.119	1217.90
(2–8)P(16)	[2,15]	1612.39	0.138	1218.52
(2–9)R(14)	[2,15]	1617.42	0.103	1218.52
(0–5)R(2)	[0,3]	1395.20	0.096	1219.09
(0–5)P(4)	[0,3]	1407.29	0.120	1219.09
(0–6)P(4)	[0,3]	1468.39	0.070	1219.09

Notes.

^a Transitions are for the $B^1\Sigma_u^+-X^1\Sigma_g^+$ H₂ band system.

^b The branching ratio is the ratio of the line transition probability to the total transition probability out of state [*v*',*J*'], $B_{mn} = A_{n'v',J' \rightarrow v'',J''} / A_{n'v',J'}$.

^c Blended with Si IV λ_{lab} = 1402.77 Å in some targets.

France et al. 2010). While we concentrate on the $\langle R_{H_2} \rangle_{[1,7]}$, the $\langle R_{H_2} \rangle_{[1,4]}$ distribution is qualitatively similar. We do not compute $\langle R_{H_2} \rangle$ for targets with inclination angles $< 15^\circ$; the small radial component of the H₂ velocity vector makes the derived radii very sensitive to uncertainties in the disk geometry. We also do not compute $\langle R_{H_2} \rangle$ for the only unambiguously outflow-dominated source in the sample, RW Aur (Section 4.2.1). The impact of a second, weaker outflow emission component will bias our results toward smaller H₂ radii in some targets, but a single component dominates the majority of our sources and we therefore adopt a single emission component in order to facilitate a uniform spectral analysis.

A knowledge of the inner disk radius, R_{in} , is important for understanding the star–disk interaction. In order to avoid complications from outflows or blending from adjacent weaker

H₂ transitions, we do not measure $R_{in}(H_2)$ from half-width zero-intensities (e.g., Brittain et al. 2009). Instead, we adopt the definition of R_{in} suggested by Salyk et al. (2011a) for mid-IR CO emission from the inner disk, where R_{in} is the Keplerian semi-major axis corresponding to $1.7 \times$ half-width at half-maximum (HWHM) of the Gaussian line fit. This choice leads to the relation between the average H₂ radius and the inner H₂ radius, $\langle R_{H_2} \rangle_{[1,7]} = 2.89 R_{in}(H_2)$. $R_{in}(H_2)$ is given with $\langle R_{H_2} \rangle_{[1,7]}$ in Table 4.

4. DISCUSSION

There are numerous indicators of the gas and dust content of a young protoplanetary system. Three important observables are the warm dust content of the inner disk, the presence of circumstellar gas, and signs of active accretion. Our *HST* observations provide measurements of the last two, while the first has been extensively studied in the IR. The combination of low spectral resolution and large instrumental backgrounds that has complicated the detection and analysis of H₂ in previous UV surveys has largely been remedied with the installation of COS. The large transition probabilities of the H₂ electronic band systems and the lack of photospheric emission at $\lambda < 1700$ Å in low-mass stars make fluorescent H₂ one of the most sensitive indicators for the presence of molecular gas in the inner ~ 10 AU of young circumstellar disks.

Accretion shocks are a significant source of hot gas in accreting systems, observed as UV and X-ray emission lines in excess of what can be attributed to magnetospheric activity alone (Calvet & Gullbring 1998; Johns-Krull et al. 2000; Günther & Schmitt 2008). Specifically, excess emission from neutral hydrogen (line formation temperature $T_{form} \sim 10^4$ K, observed as Ly α and H α emission) and the C³⁺ ion ($T_{form} \sim 10^5$ K, observed through the $\lambda\lambda 1548, 1550$ C IV resonance doublet) correlate well with both the mass accretion rate and the H₂ emission from the system (Johns-Krull et al. 2000). This supports a symbiotic picture where gas-rich disks provide fuel for active accretion, and that accretion dominates the production of the Ly α photons that make the H₂ disk detectable.

The total H₂ luminosity is compared with the Ly α and C IV luminosities in Figure 6. The general trend follows the expected relation that systems with larger $L(\text{Ly}\alpha)$ and $L(\text{C IV})$ are actively accreting gas-rich disks. Ly α fluxes are only available for about half of our sample (see Schindhelm et al. 2012b), and we interpolate (or extrapolate) the strong correlation between $F(\text{Ly}\alpha)$ and $F(\text{H}_2)$ to estimate $L(\text{Ly}\alpha)$ for the remaining objects. The direct measurements are shown as black squares in Figure 6, the interpolated (extrapolated) values are shown in green, and upper limits are indicated in red. The correlation between $L(\text{H}_2)$ and $L(\text{C IV})$ has a spread of ~ 1 – 1.5 orders of magnitude in $L(\text{H}_2)$ at a given C IV luminosity. This spread may be partially due to uncertainties in the distance and reddening correction used to derive the luminosities, disks/outflows with differing amounts of molecular gas, and intrinsic variations in the C IV flux. In the following subsections, we combine our molecular and atomic tracers to constrain the properties of H₂ in the circumstellar environments of these systems.

4.1. Evolution of the H₂ Luminosity and Reprocessing of the Ly α Radiation Field

The dissipation of inner dust disks (at $a < 1$ AU) is thought to be mostly complete by ≈ 6 Myr (e.g., Haisch et al. 2001; Wyatt 2008, and references therein). If the molecular gas and dust are

Table 3
Reddening-corrected H₂ Progression Fluxes for the CTTS Sample

Target	$F_{[3,13]}$ (λ 1213.36)	$F_{[4,13]}$ (λ 1213.68)	$F_{[3,16]}$ (λ 1214.47)	$F_{[4,4]}$ (λ 1214.78)	$F_{[1,7]}$ (λ 1215.73)	$F_{[1,4]}$ (λ 1216.07)	$F_{[3,0]}$ (λ 1217.04)	$F_{[0,1]}$ (λ 1217.21)	$F_{[0,2]}$ (λ 1217.64)	$F_{[2,12]}$ (λ 1217.90)	$F_{[2,15]}$ (λ 1218.52)	$F_{[0,3]}$ (λ 1219.09)
AA Tau	...	17.57 ± 8.79	11.00 ± 3.51	7.29 ± 4.84	29.02 ± 1.83	55.59 ± 9.11	5.79 ± 1.57	30.95 ± 4.75	30.90 ± 5.75	9.60 ± 0.50	...	1.06 ± 0.49
AK Sco	4.74 ± 2.37	10.23 ± 4.40	21.95 ± 2.90	...	0.41 ± 8.97	17.63 ± 8.82	6.63 ± 1.87	2.56 ± 1.28	...
BP Tau	...	26.45 ± 13.22	18.50 ± 3.32	30.49 ± 20.34	50.92 ± 4.30	85.91 ± 14.66	5.25 ± 1.53	27.70 ± 4.37	33.83 ± 18.00	6.53 ± 1.40	1.22 ± 0.61	2.86 ± 0.90
CS Cha	7.85 ± 2.53	28.53 ± 14.26	56.78 ± 6.01	43.76 ± 5.92	70.30 ± 6.19	159.50 ± 9.50	19.18 ± 3.02	117.55 ± 6.88	82.83 ± 17.70	24.64 ± 4.47	3.19 ± 1.60	6.34 ± 1.73
CV Cha	...	74.83 ± 37.42	...	57.55 ± 28.77	8.47 ± 69.44	89.96 ± 30.62	199.24 ± 88.07	40.98 ± 20.49
DE Tau	2.18 ± 0.18	5.12 ± 2.56	14.12 ± 1.30	26.94 ± 4.37	1.64 ± 1.31	10.21 ± 1.96	21.01 ± 11.67	2.82 ± 0.67	...	1.52 ± 0.76
DF Tau A	8.80 ± 4.40	7.61 ± 3.80	13.06 ± 4.27	6.73 ± 3.36	25.10 ± 3.95	47.41 ± 8.01	5.95 ± 3.45	59.75 ± 9.87	128.54 ± 6.82	65.52 ± 8.28	19.15 ± 4.83	20.78 ± 3.20
DK Tau A	3.77 ± 0.18	4.62 ± 2.31	21.50 ± 0.95	33.84 ± 4.85	1.54 ± 0.77	10.77 ± 0.31	11.38 ± 0.91	2.88 ± 0.16	...	0.68 ± 0.34
DM Tau	2.43 ± 0.38	2.40 ± 1.20	4.23 ± 0.13	2.81 ± 0.11	3.43 ± 0.15	7.28 ± 0.27	0.94 ± 0.22	6.84 ± 0.80	6.95 ± 1.57	3.20 ± 0.35	0.58 ± 0.29	0.47 ± 0.28
DN Tau	...	23.27 ± 11.64	...	47.89 ± 23.95	85.33 ± 38.53	194.53 ± 21.15	128.83 ± 64.42	77.07 ± 6.55	262.25 ± 285.10	44.37 ± 22.18	...	34.75 ± 13.19
DR Tau	...	4661.33 ± 2330.67	1934.36 ± 967.18	2839.96 ± 1419.98	8137.43 ± 338.12	13398.62 ± 2751.21	417.09 ± 208.54	6879.08 ± 997.43	14108.95 ± 4429.67	5220.44 ± 3289.99	...	2593.34 ± 2621.59
GM Aur	1.65 ± 0.65	1.96 ± 0.98	4.85 ± 1.20	8.54 ± 5.61	7.15 ± 0.81	15.98 ± 1.19	4.25 ± 4.58	11.81 ± 2.01	15.20 ± 0.69	5.04 ± 0.93	1.49 ± 0.75	0.95 ± 0.30
HD 104237	1615.43 ± 1687.65	...	414.96 ± 141.01	...	947.82 ± 776.47	266.20 ± 82.25	900.44 ± 450.22	138.61 ± 69.31	294.78 ± 147.39	284.24 ± 590.23	1017.59 ± 508.80	113.33 ± 56.67
HD 135344B	0.06 ± 0.03	5.86 ± 2.93	2.75 ± 0.29	4.54 ± 1.37	8.75 ± 0.42	23.40 ± 1.81	0.52 ± 0.08	6.43 ± 0.96	8.06 ± 4.83	1.88 ± 0.68	...	2.29 ± 0.22
HN Tau A	...	3.89 ± 1.94	3.57 ± 1.79	2.37 ± 1.18	10.08 ± 0.19	20.61 ± 1.27	2.26 ± 1.77	12.03 ± 2.36	19.63 ± 3.35	5.64 ± 0.93	...	1.20 ± 0.60
IP Tau	0.25 ± 0.02	...	2.31 ± 0.65	3.28 ± 0.35	9.45 ± 4.73	0.28 ± 0.10	1.19 ± 0.60	0.17 ± 0.08
LkCa 15	...	8.81 ± 4.40	5.93 ± 0.51	5.37 ± 2.68	16.11 ± 0.67	31.33 ± 2.89	1.41 ± 0.76	11.47 ± 1.71	17.17 ± 4.12	4.83 ± 1.39	...	1.21 ± 0.60
RECX 11	0.14 ± 0.07	1.58 ± 0.79	0.66 ± 0.17	0.97 ± 0.48	2.95 ± 0.18	7.02 ± 0.13	0.19 ± 0.16	1.18 ± 0.12	1.83 ± 0.81	0.15 ± 0.06
RECX 15	0.51 ± 0.26	1.53 ± 0.77	1.22 ± 0.35	1.31 ± 0.32	4.93 ± 0.24	14.03 ± 1.56	0.91 ± 0.10	7.09 ± 0.64	11.11 ± 0.50	3.90 ± 0.48	0.76 ± 0.38	0.49 ± 0.38
RU Lupi	1.29 ± 0.64	...	0.00 ± 15.69	5.62 ± 1.71	12.03 ± 0.82	26.72 ± 1.67	1.05 ± 0.47	14.48 ± 1.97	39.38 ± 54.30	5.81 ± 1.61	...	1.53 ± 0.77
RW Aur	67.90 ± 38.45	19.07 ± 9.54	429.17 ± 214.59	958.98 ± 158.68	34.40 ± 22.45	413.61 ± 36.24	1197.42 ± 957.90	364.59 ± 77.01	117.39 ± 58.69	71.68 ± 35.84
SU Aur	...	8.85 ± 4.42	5.74 ± 3.20	5.39 ± 2.70	19.20 ± 0.91	50.87 ± 6.83	1.69 ± 0.30	18.99 ± 1.76	35.55 ± 14.68	7.17 ± 3.43	...	1.51 ± 0.75
SZ 102	12.59 ± 6.29	26.36 ± 2.92	79.95 ± 6.44	10.22 ± 3.97	81.62 ± 3.01	142.33 ± 26.73	43.76 ± 4.69	5.60 ± 0.45	7.68 ± 4.88
TW Hya	23.59 ± 4.86	26.03 ± 13.02	31.84 ± 5.54	15.40 ± 34.14	37.98 ± 2.43	84.69 ± 8.07	8.20 ± 13.83	72.55 ± 21.68	90.98 ± 20.78	43.21 ± 7.50	5.93 ± 2.96	6.59 ± 0.84
UX Tau A	0.49 ± 0.24	7.32 ± 3.66	3.74 ± 0.57	4.53 ± 0.10	7.48 ± 0.22	17.29 ± 0.39	0.73 ± 0.30	5.55 ± 0.73	4.95 ± 0.21	1.24 ± 0.06	...	0.32 ± 0.16
V4046 Sgr	4.60 ± 0.09	2.97 ± 1.49	19.03 ± 1.08	15.47 ± 6.92	35.45 ± 0.94	81.47 ± 4.35	4.13 ± 0.99	34.69 ± 2.27	31.91 ± 5.75	9.62 ± 1.23	...	0.97 ± 0.98
V836 Tau	...	12.98 ± 6.49	19.69 ± 8.16	24.07 ± 22.86	59.43 ± 3.25	154.08 ± 18.64	8.22 ± 3.71	33.04 ± 3.11	26.88 ± 2.72	3.82 ± 1.91

Notes. The pumping wavelength is listed below the progression flux label. Progression fluxes are listed in units of 10^{-14} erg cm⁻² s⁻¹.

(This table is available in its entirety in a machine-readable form in the online journal. A portion is shown here for guidance regarding its form and content.)

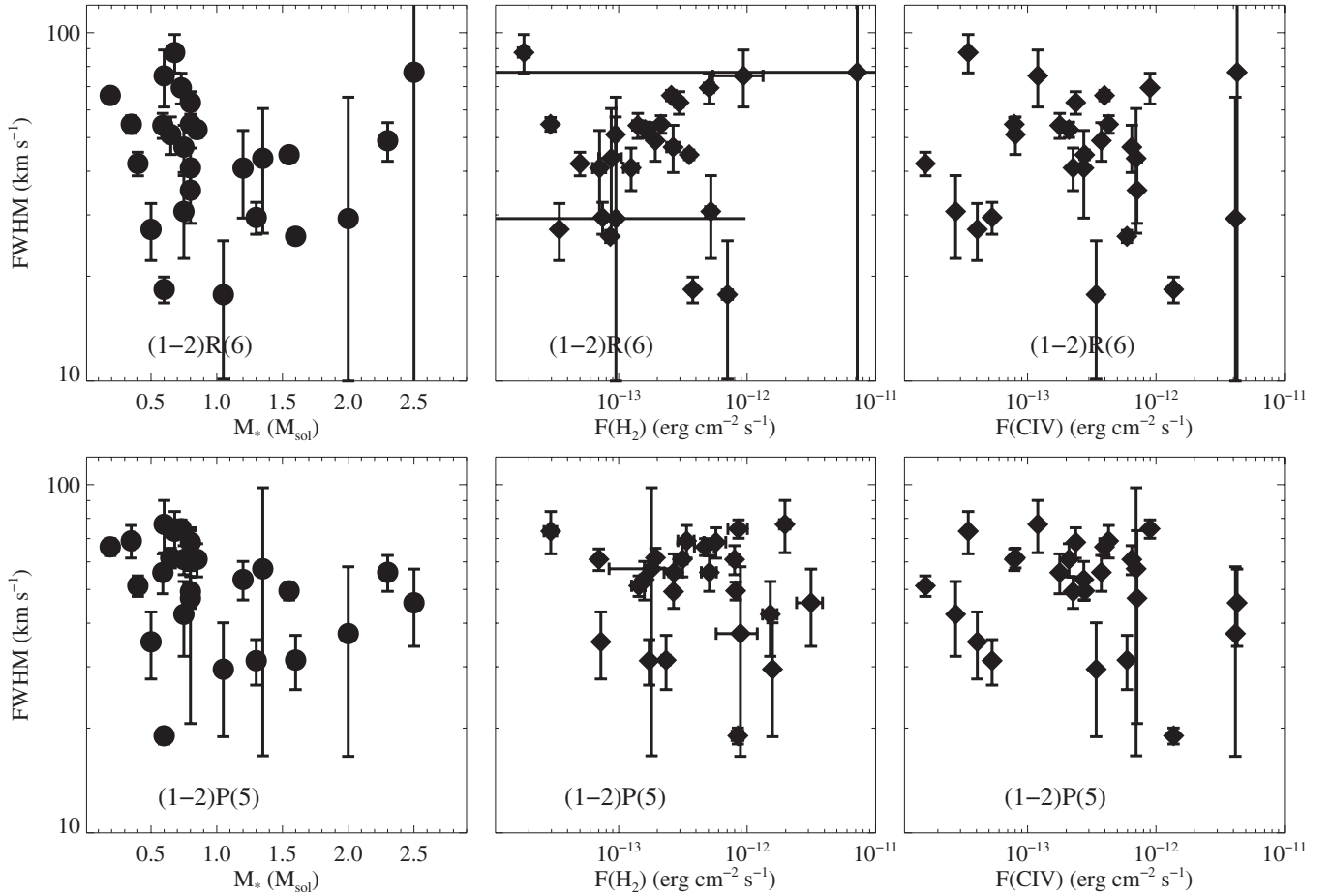


Figure 5. Average H₂ FWHM is compared with the stellar mass, the progression flux ($F_m(\text{H}_2)$), and the C IV flux ($F(\text{CIV})$) for two progressions: [1,7] (pumped through the (1–2) R(6) $\lambda_{\text{lab}} = 1215.73 \text{ \AA}$ transition) and [1,4] (pumped through the (1–2) P(5) $\lambda_{\text{lab}} = 1216.07 \text{ \AA}$ transition). The H₂ emission line FWHMs are uncorrelated with the stellar mass, $F_m(\text{H}_2)$, or $F(\text{CIV})$.

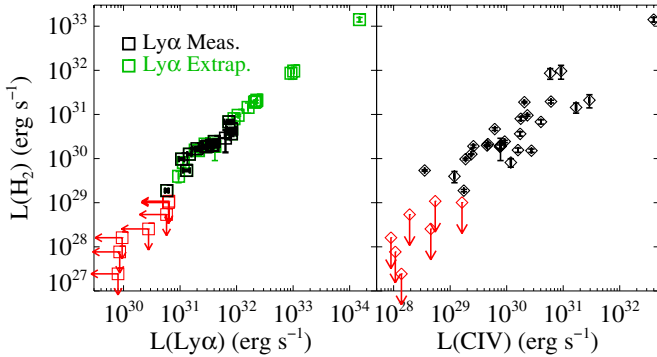


Figure 6. Comparison of the hot gas ($\log_{10}(T_{\text{form}}) \sim 4\text{--}5$) and molecular gas emission from the TTSs studied here. The Ly α and C IV emission is produced in the protostellar atmosphere through a combination of magnetic activity and magnetically funneled accretion. The H₂ resides in the circumstellar disk and, in some cases, extended outflows excited by Ly α photons. The H₂ luminosity is the summed luminosity of the 12 progressions listed in Table 2, representing $\gtrsim 80\%$ of the total H₂ luminosity (depending on the specific Ly α -pumping profile). Targets with H₂ upper limits are plotted in red. The black squares in the left plot are our H₂ measurements and the empirically determined Ly α fluxes presented by Schindhelm et al. (2012b). The green squares are an extrapolation of the $F(\text{H}_2)$ vs. $F(\text{Ly}\alpha)$ relationship.

(A color version of this figure is available in the online journal.)

coupled, we would expect to observe a decrease in the H₂ content as a function of system age. The evolution of the H₂ luminosity is plotted in the top panel of Figure 7. The H₂ detections are shown in black and the non-detections in red. The total H₂ luminosity

decreases with time, in agreement with the findings of Ingleby et al. (2009, 2011a). However, the large scatter in the relation prevents one from inferring a characteristic timescale for this decrease. The dominant sources of uncertainty in this relation are the correlated errors on the age and extinction. The observed decrease in $L(\text{H}_2)$ as a function of time does not necessarily correspond to a monotonic decrease in the H₂ content. We expect that the Ly α luminosity should track the accretion rate (e.g., Fang et al. (2009) demonstrate the correlation between accretion and H Balmer emission); therefore as the accretion rates decline over time (Armitage et al. 2003; Sicilia-Aguilar et al. 2010), the associated reduction in Ly α emission could mimic the effect of H₂ dissipation with age. The true situation is likely a combination of these effects: gas disk dissipation leads to lower accretion rates that in turn produce fewer Ly α photons to pump the observed fluorescence.

The lower panel in Figure 7 shows the ratio of the H₂ flux and the Ly α flux as a function of system age for the 14 objects with computed Ly α fluxes (Schindhelm et al. 2012b). This plot shows the fraction of the stellar + shock Ly α that is reprocessed by H₂. The actual reprocessing factor is $\eta F(\text{H}_2)/F(\text{Ly}\alpha)$, where η is a correction factor to account for anisotropies in the system geometry and fluorescent radiative transfer (Wood et al. 2002; Wood & Karovska 2004). In the case of isotropic emission, η is simply the geometric filling fraction of the H₂, as seen by the Ly α photons. For this comparison (and for the computation of $L(\text{Ly}\alpha)$ in Figure 6), we have assumed $\eta = 1$. For sources where the majority of the H₂ resides in a flattened disk, η is most

Table 4
Molecular and Atomic Emission Line Parameters

Target	FWHM _[1,7] ^a (km s ⁻¹)	$\langle R_{H_2} \rangle_{[1,7]}$ ^a (AU)	R_{in} ^b (AU)	FWHM _{CO} ^c (km s ⁻¹)	n_{13-31}	$L(H_2)$ ^a (10 ²⁹ erg s ⁻¹)	$L(Ly\alpha)$ ^d (10 ²⁹ erg s ⁻¹)	$L(C\,IV)$ ^e (10 ²⁹ erg s ⁻¹)
AA Tau	62 ± 4	0.69 ± 0.08	0.24	92	-0.51	46.7 ± 3.1	818.5 ± 146.6	6.1
AK Sco	57 ± 35	1.25 ± 0.77	0.43	8.1 ± 1.3	114.4	11.8
BP Tau	70 ± 6	0.13 ± 0.02	0.05	87	-0.58	68.0 ± 7.4	731.7 ± 129.7	40.3
CS Cha	18 ± 7	9.00 ± 4.55	3.11	...	2.89	189.9 ± 12.9	2076.7	20.6
CV Cha	22 ± 30	4.75 ± 3.88	1.64	...	-0.27	139.1 ± 35.5	1540.7	169.1
DE Tau	55 ± 6	0.23 ± 0.04	0.08	...	-0.12	20.1 ± 3.0	361.2 ± 106.0	7.8
DF Tau A ^f	64 ± 7	0.16 ± 0.03	0.06	79	-1.09	95.7 ± 4.6	1064.7	23.2
DK Tau A ^f	55 ± 2	0.24 ± 0.02	0.08	...	-0.81	21.3 ± 1.2	276.7	4.6
DM Tau	27 ± 5	0.80 ± 0.24	0.28	...	1.30	9.7 ± 0.7	106.5 ± 11.7	1.9
DN Tau	71 ± 19	0.09 ± 0.04	0.03	...	-0.43	210.6 ± 67.8	2279.5	290.8
DR Tau	35 ± 7	2.09 ± 0.62	0.72	29	-0.40	14117.7 ± 1590.0	149385.1	3986.7
GM Aur	41 ± 11	1.68 ± 0.65	0.58	47	1.76	18.5 ± 1.8	286.1 ± 70.4	7.6
HD 104237	94 ± 77	0.10 ± 0.07	0.03	964.4 ± 315.6	10239.6	91.6
HD 135344B	26 ± 1	47	...	15.1 ± 1.3	212.0	27.4
HN Tau A ^f	61 ± 17	0.47 ± 0.18	0.16	...	-0.44	19.1 ± 1.1	307.2 ± 60.3	2.6
IP Tau ^f	102 ± 29	0.17 ± 0.07	0.06	...	-0.11	4.0 ± 0.2	94.0	1.2
LkCa 15	53 ± 3	0.62 ± 0.06	0.21	...	0.62	24.4 ± 1.3	403.4 ± 66.4	9.2
RECX 11	54 ± 3	0.85 ± 0.08	0.29	1.9 ± 0.1	58.3 ± 3.9	1.7
RECX 15 ^f	41 ± 4	0.62 ± 0.10	0.21	5.4 ± 0.3	130.6 ± 17.8	0.4
RU Lupi	40 ± 2	0.30 ± 0.03	0.10	24	...	27.2 ± 15.2	635.3 ± 148.3	12.0
RW Aur A ^g	-0.54	860.7 ± 228.9	9169.5	58.9
SU Aur	49 ± 6	2.67 ± 0.58	0.92	121	0.74	36.3 ± 4.0	811.4 ± 191.4	17.3
SZ 102	47 ± 7	196.2 ± 13.8	2182.4	60.8
TW Hya	18 ± 2	17	...	16.8 ± 2.0	199.6 ± 34.3	17.0
UX Tau A	29 ± 3	1.76 ± 0.33	0.61	21	1.83	12.6 ± 0.3	146.3 ± 12.3	2.4
V4046 Sgr	45 ± 1	0.95 ± 0.06	0.33	19.8 ± 0.9	383.3 ± 42.1	4.5
V836 Tau	47 ± 20	0.99 ± 0.50	0.34	...	-0.45	80.2 ± 7.3	900.5	17.7
HBC 427 ^h	≤0.5	≤57.7	0.2
LKCa 19	≤1.1	≤63.6	0.5
LKCa 4	≤1.0	≤62.6	1.6
RECX 1	≤0.3	≤27.7	0.5
TWA 13A	≤0.1	≤9.2	0.1
TWA 13B	≤0.2	≤10.2	0.1
TWA 7	≤0.0	≤8.6	0.1

Notes.

^a Average FWHM and average H₂ radius (see Section 3.2) were calculated from four lines of the H₂ $B^1\Sigma_u^+ - X^1\Sigma_g^+(1-v'')$ R(6)+P(8) progression. The H₂ luminosity is the sum of the 12 progressions measured in this work (Table 2).

^b Inner H₂ radius, defined as $R_{in} = GM_* (\sin(i)/(1.7 \times \text{FWHM}_{[1,7]}))^2$.

^c CO line widths taken from Salyk et al. (2011a) and Bast et al. (2011).

^d H I Ly α luminosities with error bars were calculated from the Ly α fluxes presented by Schindhelm et al. (2012b). Values without error bars were extrapolated from the relationship between $F(H_2)$ and $F(Ly\alpha)$.

^e Measurement error on the C IV flux is taken as 5%.

^f Targets where molecular outflows may contribute to the observed H₂ line width.

^g Strong molecular outflows in RW Aur contaminate the Gaussian fitting (see Figures 3(b) and 8).

^h Targets below the double line do not show measurable H₂ emission in their far-UV spectra.

likely less than one (Herczeg et al. (2004) found $\eta \approx 0.25$ in model fits to the spectrum of TW Hya), while for sources with a significant outflow component η may be ~ 1 . Yang et al. (2011) and France et al. (2012) present analyses of H₂ absorption lines imposed on the Ly α profiles of the CTTSs V4046 Sgr, DF Tau, and AA Tau, systems with both high and low inclinations. This implies that at least some portion of the H₂ in these systems has an Ly α covering fraction of near unity, suggesting that $\eta \sim 1$ even in some disk-dominated systems. Furthermore, in cases where Ly α has been scattered out of our line of sight or self-absorption redistributes the fluorescence to the higher v'' levels we use to determine $F(H_2)$, η can be > 1 (Wood et al. 2002). In the absence of a more sophisticated radiative transfer treatment of each system individually, we assume $\eta = 1$ for the present analysis.

The total Ly α flux is the full, unabsorbed Ly α profile as it is emitted from the immediate stellar environment. Figure 7 shows that the ratio of the total emitted Ly α flux that is reprocessed by H₂ is $6.2\% \pm 2.1\%$. A more meaningful measure of the degree of H₂ reprocessing is the ratio of incident Ly α that arrives at the molecular material. The Ly α profile will experience some degree of absorption in the circumstellar environment prior to reaching the molecules (Wood & Karovska 2004; Herczeg et al. 2004; Schindhelm et al. 2012a). Using the incident Ly α profile observed by the H₂, we find that the reprocessing fraction ($\eta F(H_2)/F(Ly\alpha)$) is $11.5\% \pm 1.8\%$. Therefore, modulo the factor of η , we infer that H₂ is capable of reprocessing $> 10\%$ of the incident Ly α flux. This is interesting because the H₂ (1) will isotropically redistribute the Ly α photons and (2) represents a means for transferring Ly α photons out of the Ly α line core and

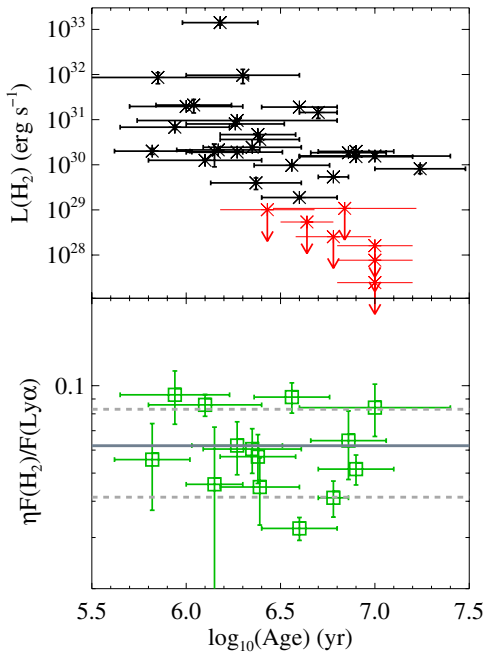


Figure 7. We plot the time evolution of the H_2 luminosity from the protoplanetary environment (top). The H_2 detections are shown in black and the non-detections in red. The lower plot presents a measure of the H_2 reprocessing of the stellar $\text{Ly}\alpha$ emission, expressed as the H_2 flux divided by the empirically determined photoexciting $\text{Ly}\alpha$ fluxes (Schindhelm et al. 2012b). η is a correction for radiative transfer effects and the anisotropy of the system, set here to $\eta = 1$ (see Section 4.1). The average H_2 reprocessing fraction of the total $\text{Ly}\alpha$ profile is $6.2\% \pm 2.1\%$, assuming $\eta = 1$, shown with solid (mean) and dashed (1σ) gray lines in the lower panel.

(A color version of this figure is available in the online journal.)

redistributing them across the $1000 \lesssim \lambda \lesssim 1650 \text{ \AA}$ bandpass. Additionally, H_2 scattering is a means for redirecting $\text{Ly}\alpha$ photons initially on a grazing incidence trajectory, increasing the far-UV radiation penetration depth. This will significantly alter the radiative transfer of this fraction of the $\text{Ly}\alpha$ energy as it diffuses outward and downward through the disk (Fogel et al. 2011; Bethell & Bergin 2011). The transfer of these H_2 -redistributed $\text{Ly}\alpha$ photons will be regulated by circumstellar grains, and this process will add power to discrete wavelengths in the far-UV spectrum that propagates toward the disk midplane, possibly perturbing disk chemistry in regions of active planet formation.

4.2. Spatial Distribution of H_2

4.2.1. H_2 Outflows

A single Gaussian emission line describes many of the observed velocity profiles; however several targets show evidence for molecular outflows in the form of additional red/blueshifted H_2 emission. Beck et al. (2008) presented an outflow-selected sample of CTTs that display spatially extended near-IR rovibrational H_2 spectra. Furthermore, Pontoppidan et al. (2011) have found slow ($5\text{--}10 \text{ km s}^{-1}$), weakly collimated molecular winds to be common in CO spectra of CTTs, and varying contributions from these winds/outflows could be responsible for the blueshifted H_2 that is observed toward some systems. The COS observations of DF Tau, DK Tau, HN Tau, LkCa 15, IP Tau, RECX 15, RU Lupi, and RW Aur all display H_2 line wings extending to the blue of the stellar radial velocity. Interestingly, half of these objects are known binaries (DF Tau, DK Tau, HN Tau, and RW Aur), and this may indicate that interactions

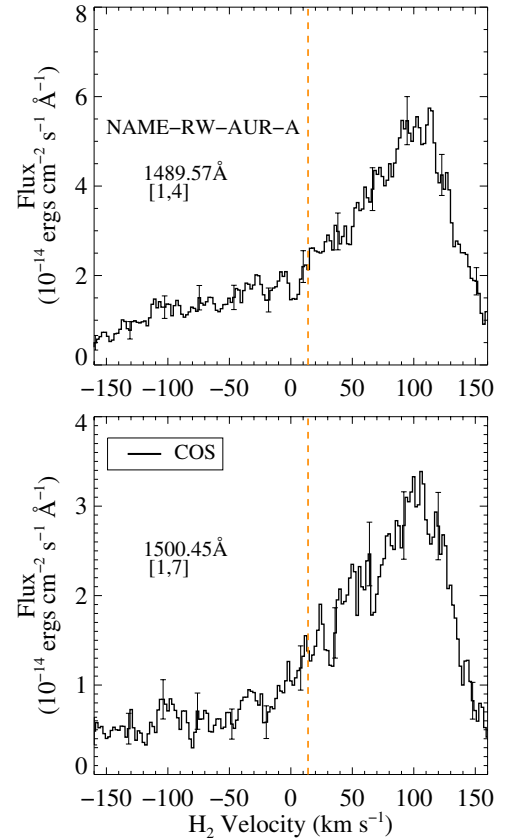


Figure 8. COS H_2 line profiles of RW Aur display a complicated kinematic behavior. Stellar variability compromises radial velocity measurements for RW Aur. We display $+14 \text{ km s}^{-1}$, the canonical stellar radial velocity (Hartmann et al. 1986), as the dashed orange line. The H_2 line profile is dominated by the redshifted outflow lobe (Melnikov et al. 2009) with an outflow velocity of $\approx 100 \text{ km s}^{-1}$.

(A color version of this figure is available in the online journal.)

with a companion star contribute to the generation of molecular outflows in CTTs. Clearly, more data are required to test this connection.

Of the targets displaying H_2 emission with extended blue wings, DF Tau, DK Tau, HN Tau, IP Tau, RECX 15, and RW Aur also have reasonably high S/N [0,1] progression emission lines in their spectra. The [0,1] line widths are statistically narrower than those from [1,7] and [1,4], also suggesting that outflow contributions to the [1,4] and [1,7] progressions are present in these targets (Walter et al. 2003). RW Aur shows the strongest outflow emission in the survey, with both redshifted and blueshifted emission observed. It is not clear that there is a narrow disk H_2 component present in this source. We show a blow-up of bright lines from the [1,7] and [1,4] progressions in RW Aur in Figure 8. RW Aur is known to have a bipolar outflow, with the red component ($v_{\text{out}} \sim +100 \text{ km s}^{-1}$) being brighter and higher density than the blue (Hirth et al. 1994; Melnikov et al. 2009). Due to the COS aperture vignetting function, the observed spectra will be dominated by the inner $\approx 1''$ of the RW Aur jet. Figure 8 shows that the H_2 emission peaks at an observed velocity $80\text{--}110 \text{ km s}^{-1}$ to the red of the stellar velocity ($+14 \text{ km s}^{-1}$; Hartmann et al. 1986), suggesting that the molecular emission arises in material that is approximately cospatial with the forbidden atomic line (e.g., $[\text{S II}] \lambda 6731$) emission (Woitas et al. 2002; Melnikov et al. 2009; Hartigan & Hillenbrand 2009). The near-IR H_2 outflow from RW Aur

is centered near $\sim +44 \text{ km s}^{-1}$ (Beck et al. 2008), significantly bluer than the peak of the far-UV H_2 velocity profile. It is not clear if this indicates a difference in the physical structure of the UV- and IR-emitting H_2 , or can be attributed to blending of low- and high-velocity gas in the lower spectral resolution near-IR data. For the remaining targets, the blue wings are relatively weak, typically only perturbations from the narrower, presumably disk-dominated H_2 velocity profiles. Further study using co-added spectra from several progressions would be useful for clarifying the outflow contribution and structure in these targets.

The observed H_2 velocity profiles of RU Lupi are puzzling. Using higher spectral resolution observations from STIS, Herczeg et al. (2005, 2006) found that essentially all of the fluorescent H_2 was contained in two blueshifted components, -12 and -30 km s^{-1} relative to the radial velocity of the star. While a blue wing is apparent in the COS observations, the emission is well fitted by a single component at the radial velocity of the star. In Figure 9, we compare the COS observations of RU Lupi (obtained in 2011 using the $2''.5$ diameter Primary Science Aperture) with the STIS observations of RU Lupi (obtained in 2000 using the $0''.2 \times 0''.06$ slit). The apparent line-center velocity shift is $\approx 15\text{--}20 \text{ km s}^{-1}$, larger than the zero-point calibration of the COS wavelength solution.¹³ Furthermore, the line shape is fundamentally different in a way that cannot be explained by resolution differences between the two instruments. In the bottom panel of Figure 9, we reconstruct a model two-Gaussian profile (solid blue line) using the fit parameters from Herczeg et al. (2006). That profile, convolved with the COS LSF at 1490 \AA (Kriss 2011), is displayed as the red dash-dotted curve. CTTSs (and in particular RU Lupi; Gahm et al. 2008) are known to be time variable; therefore it is not surprising that the peak flux has changed, but the line center and emission line shapes are not consistent.

Herczeg et al. (2006) found that the H_2 fluorescence in RU Lupi was spatially extended, although the small size of the STIS aperture makes it difficult to predict the effects of spatial extension in the larger COS aperture. An aperture offset of $\gtrsim 0''.4$ would be required for significant reduction in the instrumental resolving power, but angular extension of the H_2 -emitting region may be able to alter both the velocity centroid and the line width. In the dispersion direction, if we attribute the entire 20 km s^{-1} offset to extended emission, this leads to a $0''.2$ displacement (at the $24.3 \text{ mas pixel}^{-1}$ dispersion-direction plate scale of the G160M mode). We cannot constrain the angular extent of the RU Lupi H_2 lines in the dispersion direction, but we note that the optical forbidden line emissions ([O I] and [S II]) are extended to $\sim 0''.2$ at a position angle of $\sim 225^\circ$ (Takami et al. 2001). If the H_2 emission lines observed in the COS spectra are cospatial with the forbidden line emission, then this could produce the $\sim +20 \text{ km s}^{-1}$ velocity offset. Therefore, it is possible that spatial extension of the H_2 -emitting gas along this axis could explain the differences in line shape between the STIS and COS observations. We compared the cross-dispersion profile of the two-dimensional spectrogram of the RU Lupi observations (over the range $\Delta\lambda \sim 1420\text{--}1450 \text{ \AA}$) with that of the DA white dwarf WD 0320-539. The two spectra were centered to within 0.5 pixels ($\approx 0''.05$) in the cross-dispersion direction and had nearly identical profile FWHMs (4.5 pixels for WD 0320, 4.8 pixels for RU Lupi).

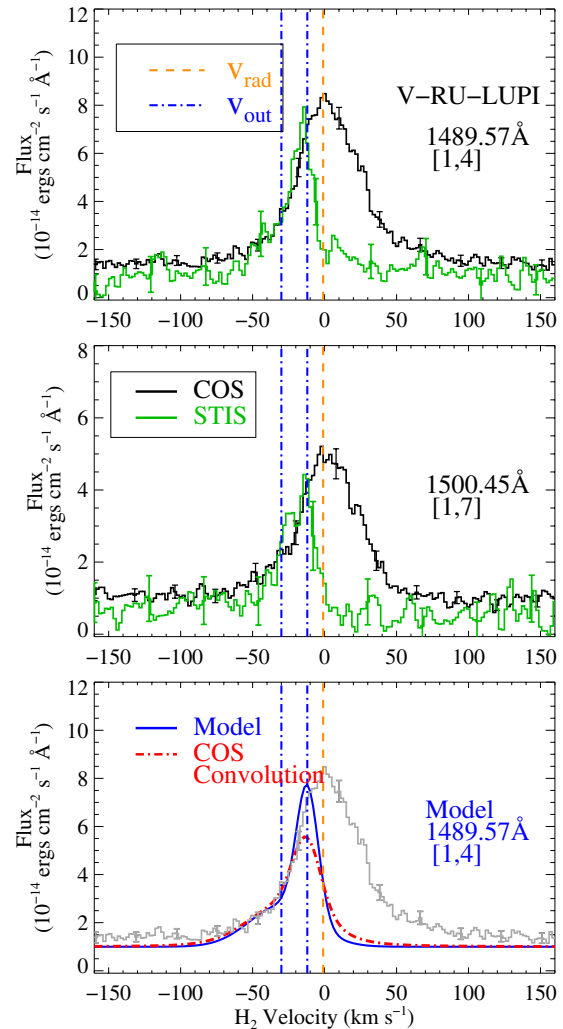


Figure 9. Comparison of archival STIS spectra of H_2 emission lines from RU Lupi (green) and new observations from COS (black). The stellar radial velocity is indicated with the orange dashed line and the outflow velocities from Herczeg et al. (2006) are shown as the dash-dotted blue lines. Strong lines from the [1,4] and [1,7] progressions are shown in the top two panels, and the bottom panel shows the two-component spectral fit for the STIS observations in blue (Herczeg et al. 2006). This profile, convolved with the 1490 \AA COS LSF is shown as the red dash-dotted line and the observed COS data are shown in gray. The COS data are consistent with the stellar radial velocity and do not display asymmetric outflow profiles as strong as was observed by STIS. This difference may be due to a physical change in the inner regions of RU Lupi or could be explained by angular extension along the dispersion axis in the COS data (Section 4.2.1). (A color version of this figure is available in the online journal.)

We conclude, therefore, that either RU Lupi has spatial extent along the dispersion axis, or the spectral profile differences between the COS and STIS epochs are caused by a physical change in the system. RU Lupi may continue to be outflow dominated; however the COS observations raise the possibility that RU Lupi was observed during an episode of strong outflow in 2000 or that the geometry has evolved such that disk illumination by $\text{Ly}\alpha$ contributed more strongly during the 2011 observations. Continued spectral monitoring of these loopy line profiles would be interesting.

4.2.2. H_2 Disks

The high S/N H_2 lines in the majority of our sample targets can be adequately described by a single Gaussian emission component at the stellar radial velocity. Bearing in mind the

¹³ Calibration of the COS wavelength solution is limited by systematic uncertainty in the far-UV detector geometric correction.

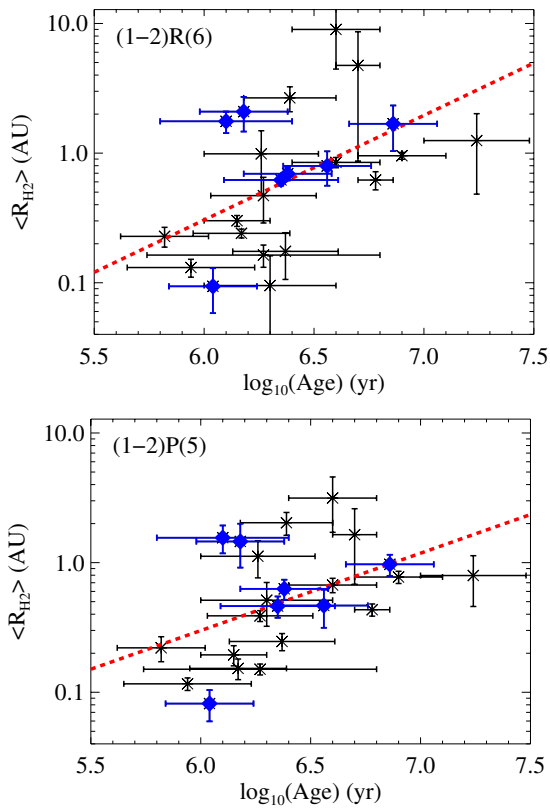


Figure 10. Time evolution of the average radial position of the H₂ emission in our sample, as defined by the Gaussian line widths of the [1,7] (pumped through the (1–2) R(6) absorption line) and [1,4] (pumped through the (1–2) P(5) absorption line) progressions (see Section 3.2 for a discussion). Only targets with disk inclinations $i > 15^\circ$ were considered. The red dashed line represents the empirical relation between the average radius of the H₂-emitting disk and the system age (Equation (3)) for the [1,7] and [1,4] progressions. The two H₂ progressions show a similar behavior with system age. The Spearman rank correlation coefficient for increasing molecular radius with system age for both H₂ progressions is ≈ 0.52 . The blue diamonds indicate targets with inclinations derived from submillimeter dust continua (Andrews & Williams 2007; Andrews et al. 2011).

(A color version of this figure is available in the online journal.)

added uncertainty introduced by blueshifted H₂ in some targets, we conclude that most of the observed fluorescent emission originates in a disk. This is in contrast with the near-IR H₂ study of Beck et al. (2008); however, that study targeted stars known to have strong outflows, which is not the case with the sample presented here. Using the velocity-resolved H₂ line profiles, $\langle R_{H_2} \rangle$ was calculated for the [1,7] and [1,4] progressions. The radial distributions as a function of system age are displayed in Figure 10. The general result is that the average location of the emitting H₂ gas in the inner disk moves outward from ~ 0.25 AU to ~ 2 AU as the system evolves from 1 to 10 Myr.

The relationship between the system age and the average H₂ radius can be characterized by the simple empirical formula

$$\log_{10} \langle R_{H_2} \rangle_{[1,7]} = 0.81 \log_{10}(\text{Age}) - 5.36, \quad (3)$$

where $\langle R_{H_2} \rangle_{[1,7]}$ is in AU and the age is in years. The coefficients in Equation (3) [-5.36 ± 1.91 , 0.81 ± 0.30] are computed from a χ^2 minimization of a linear function of $\log_{10}(\text{Age})$ and $\log_{10} \langle R_{H_2} \rangle_{[1,7]}$. The Spearman rank correlation coefficient for increasing molecular radius with system age is 0.52 with a deviation from zero of 1.1×10^{-2} , meaning that there is a relatively low probability that $\log_{10}(\text{Age})$ and $\log_{10} \langle R_{H_2} \rangle_{[1,7]}$ are

uncorrelated. Targets with disk inclinations derived from submillimeter dust continuum observations (Andrews & Williams 2007; Andrews et al. 2011) are plotted as the blue diamonds in Figure 10. There is a large spread in the distribution of $\langle R_{H_2} \rangle$ with age. We suggest that in addition to contamination by outflows, uncertainties in the stellar mass, inclination angle, and stellar age all contribute to the dispersion in this correlation. With the exception of CS Cha (Section 4.3), the H₂ in all disks is concentrated at $a \lesssim 3$ AU.

The weak trend toward larger radii as a function of age suggests a scenario where the average molecular emission radius moves to beyond ≈ 1 AU in about 10 Myr. It is not immediately clear how to interpret this result, and we remind the reader of the ingredients necessary to produce H₂ fluorescence in a disk. The H₂ opacity must be high enough to absorb a significant number of Ly α photons, requiring both appreciable column densities and a sufficient population of H₂ in excited rovibrational states. The latter requires a hot ($T(\text{H}_2) \gtrsim 2000$ K) molecular layer, possibly with a contribution by intense illumination from the $\lambda \leq 1120$ Å continuum from the central star + accretion shocks (Nomura et al. 2007; France et al. 2012). The second major requirement for observable fluorescence is a geometry where the disk subtends a substantial angular cross-section of the Ly α -emitting area; that is, the disk must be sufficiently flared in order to intercept enough Ly α photons to excite the observed emission. The observation of larger H₂ radii as a function of time suggests that one or more of these criteria are not being met in the inner ≈ 1 AU in the more evolved systems. It may be that the hot H₂ is in the process of dissipating from this region, possibly due to dynamical clearing by a protoplanet, enhanced H₂ dissociation as this region is less shielded by grains, or photoevaporation by energetic radiation from the central star. Alternatively, this result may indicate that the flaring angle in the inner disk is decreasing across our sample, suggesting an evolution of the vertical structure of the disk on timescales of a few Myr. Improved stellar masses and ages, and larger samples of well-determined disk inclinations, would allow better characterization of the relation (or lack thereof) between molecular radius and age, enabling a better understanding of the evolution of inner gas disks.

4.2.3. Comparison with Near-IR H₂ Emission

Quadrupole rovibrational line emission from H₂ (most notably the (1–0) S(1) $\lambda 2.1$ μm line) has been detected around several CTTSs (Bary et al. 2003, 2008; Itoh et al. 2003; Carmona et al. 2007). While the number of objects available for direct comparison is small, it seems that the Ly α -pumped H₂ emission arises interior to the near-IR emission lines (although see Section 4.3 for the case of the transitional disk CS Cha). Typical emission line widths for the near-IR H₂ sample presented in Bary et al. (2008) are $\text{FWHM} \leq 20$ km s^{−1}, and are thought to originate at radial distances of a few to a few tens of AU. Similarly, Bary et al. (2003) observed (1–0) S(1) emission in LkCa 15 with $\text{FWHM} \leq 14$ km s^{−1} and suggested that the emitting gas was located between 10 and 30 AU from the star. This is a factor of ≈ 4 narrower than the $\text{FWHM}_{[1,7]} = 53 \pm 3$ km s^{−1} that we observe in the LkCa 15 UV spectrum.

RECX 15 is the only disk in the η Cha region to emit a measurable flux of H₂ in the (1–0) S(1) line (Ramsay Howat & Greaves 2007). The near-IR H₂ line widths (18 ± 1.2 km s^{−1}) are a factor of ≈ 2.3 smaller than measured in the COS spectra of RECX 15 (41 ± 4 km s^{−1}), although we note that outflows do contribute to the RECX 15 ultraviolet H₂ spectra. The near-IR

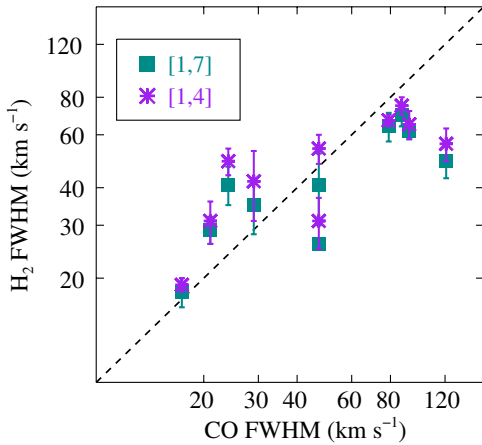


Figure 11. Comparison of the emission line FWHMs of H₂ (this work) and CO (Salyk et al. 2011a; Bast et al. 2011). The squares are the Gaussian line widths of the [1,7] progression and the stars are the Gaussian line widths of the [1,4] progression. The dashed line represents the expected correlation if the H₂ and CO line widths are the same.

(A color version of this figure is available in the online journal.)

H₂ emission from disks is typically interpreted as disk surface gas excited by energetic radiation. Including the effects of grain grown, UV, and X-ray illumination, Nomura et al. (2007) have demonstrated that gas temperatures in the range 1500–3000 K can be maintained in the disk surface to radial distances of ≈ 10 AU from the central star; therefore the excitation conditions necessary to both produce near-IR emission and to enable Ly α pumping appear to exist to at least this radius. However, the fluorescent ultraviolet emission is dominated by H₂ nearest to the source of Ly α photons.

4.2.4. Comparison with CO Emission

Comparing the line widths of different molecular species can provide an observational constraint on the composition and physical structure of inner gas disks. Spectral observations of the 4.7 μm fundamental band CO emission are a widely used tracer for this material (Salyk et al. 2008, 2009), and understanding the molecular structure and the degree to which various spectral diagnostics trace the same gas are useful toward a more complete picture of the planet-forming regions around CTTSs. Figure 11 shows a comparison of the Gaussian FWHMs of CO and H₂ for the subsample of our targets that have been observed by high-resolution mid-IR spectrographs (Salyk et al. 2011a; Bast et al. 2011). The emission line widths from the [1,7] and [1,4] H₂ progressions are self-consistent in all cases and approximately equal the CO line widths up to FWHM ≈ 60 km s⁻¹. At larger CO line widths, the H₂ FWHMs do not exceed 70–80 km s⁻¹, which may indicate a physical boundary condition inside of which H₂ is subject to collisional and/or photodissociation.

The inner radii of the H₂ and CO disks can also be compared directly. The calculated H₂ inner radii are presented in Table 4, and Figure 12 compares the ultraviolet H₂ (UV-H₂) and infrared CO (IR-CO) radii (Salyk et al. 2011a); the dashed horizontal line represents a one-to-one relation. With one exception, $R_{\text{in}}(\text{H}_2)$ and $R_{\text{in}}(\text{CO})$ are the same to within a factor of three. The agreement between the two molecules is rather remarkable given that we are comparing different species, excited by different mechanisms (photoexcitation versus collisional excitation), observed at different epochs in different wavebands. The notable exception is SU Aur, whose $R_{\text{in}}(\text{H}_2)$ is approximately an order of magnitude larger than its corresponding $R_{\text{in}}(\text{CO})$, possibly

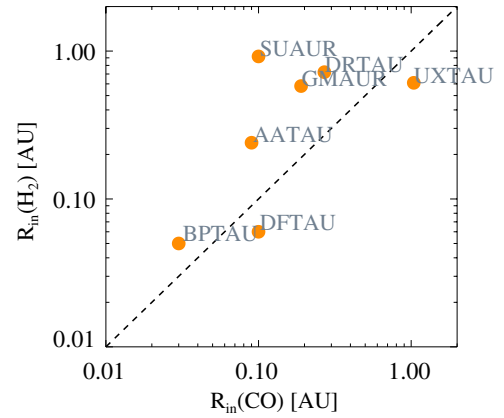


Figure 12. Comparison of inner radii (R_{in}) of the molecular disk traced by H₂ (this work) and CO (Salyk et al. 2011a). The dashed line represents the expected correlation if the H₂ and CO emission are copatial. R_{in} is defined as the Keplerian radius corresponding to an orbital velocity of $1.7 \times \text{HWHM}$ of the Gaussian line fits (Section 3.2). $R_{\text{in}}(\text{H}_2)$ is computed from the [1,7] progression for this comparison. Except in the case of SU Aur, $R_{\text{in}}(\text{H}_2)$ and $R_{\text{in}}(\text{CO})$ are the same to within a factor of three, suggesting that the observed CO and H₂ orbit at similar radii.

(A color version of this figure is available in the online journal.)

due to H₂ emission from nebulosity associated with this star. The agreement between the IR-CO emission and the UV-H₂ emission is also interesting in light of the recent discovery of large amounts of CO emission in the UV spectra of CTTSs (UV-CO; France et al. 2011b). Schindhelm et al. (2012a) present an initial survey of this emission, showing that the line widths of UV-CO are systematically narrower than those of UV-H₂. Their interpretation favors a picture where the UV-CO originates in a cooler molecular layer ($T_{\text{rot}}(\text{CO}) \sim 500$ K) at larger semi-major axes ($a \gtrsim 2$ AU) than both the UV-H₂ and the IR-CO, consistent with the results presented here.

4.3. H₂ in Transitional Disks

The majority of H₂ emission in the targets in our sample originates from $a \lesssim 3$ AU. A notable outlier from the average H₂ radii presented in Table 4 is CS Cha, which lies at significantly larger $\langle R_{\text{H}_2} \rangle_{[1,7]}$ than the rest of the disks studied here. The [1,7] line width of CS Cha is 18 ± 7 km s⁻¹, which makes it the only unresolved moderate inclination target,¹⁴ and allows us to place a lower limit on the average H₂ emission radius, $\langle R_{\text{H}_2} \rangle_{[1,7]} \geq 9$ AU. CS Cha is a transitional disk, showing the largest mid-IR spectral slope in our sample, $n_{13-31} = 2.89$ (Furlan et al. 2009; see Table 4). Modeling of the *Spitzer*-IRS mid-IR spectrum of CS Cha reveals a truncation of the inner disk dust distribution at $a \approx 43$ AU (Espaillat et al. 2007a), possibly the result of a dynamical interaction with a companion star (Guenther et al. 2007; but see also Espaillat et al. 2011). The new *HST* data presented here confirm the presence of molecular gas in the system (Bary et al. 2008), and while we cannot rule out the possibility that this gas is copatial with the dust at $a \gtrsim 40$ AU, this would imply that hot molecular gas ($T(\text{H}_2) \geq 2000$ K) exists at large radial distances from the star. Therefore, because only $N(\text{H}_2) \gtrsim 10^{18}$ cm⁻² is required to produce detectable fluorescence, this emission may originate in the tenuous molecular material in the disk gap, or if Ly α photons

¹⁴ The [1,4] line width is 29 ± 12 km s⁻¹, consistent with the [1,7] result. Bary et al. (2008) report a near-IR line width of 12.6 km s⁻¹, which would be unresolved in our COS observations.

can propagate through the gap, this emission may arise from the edge of the directly exposed wall at ~ 43 AU.

The H₂-emitting material we observe in CS Cha may be physically associated with the [Ne II] emission observed by Espaillat et al. (2007a), but that cannot be conclusively determined from the available observations. We can rule out an origin in the optically thin dust disk inside of 1 AU, as our limit on the H₂ inner disk radius in CS Cha is $R_{\text{in}}(\text{H}_2) \geq 3$ AU.

CS Cha is one example of a generic property of our sample: H₂ is common in the inner regions of accreting transitional disks ($n_{13-31} > 0.5$). In addition to CS Cha, our sample includes the well-studied transitional systems DM Tau, GM Aur, UX Tau A, LkCa 15, HD 135344B, and TW Hya (Calvet et al. 2002, 2005; Espaillat et al. 2007b). H₂ emission is found to originate inside the dust hole in these systems, $\langle R_{\text{H}_2} \rangle < R_{\text{dust}}$, consistent with the origin of the IR-CO gas in the inner regions of transitional disks (Salyk et al. 2009, 2011a) and previous observations of near-IR rovibrational emission from H₂ (Bary et al. 2008).

5. SUMMARY

We have presented the most sensitive survey of H₂ in protoplanetary environments to date. The majority of this work was made possible by the combination of large effective area and low instrumental background at moderate spectral resolution provided by the *HST*-COS. We have used this survey to measure the time evolution of both the spatial distribution and the luminosity of H₂ in young, low-mass disks for the first time. Below we summarize the primary results of this work.

1. We obtained far-UV spectra of 34 TTSSs: 27 accreting CTTSs and 7 non-accreting WTTSs. Of these, 100% of the accreting sources display a measurable amount of H₂ emission, providing direct evidence for the interaction of a strong Ly α radiation field with the molecular disk surface.
2. We found that the H₂ luminosity is well correlated with the Ly α and C IV luminosity, consistent with a scenario where gas-rich disks fuel larger accretion rates that produce energetic radiation.
3. The H₂ luminosity is observed to decline with age, although H₂-rich systems persist to ages ~ 10 Myr.
4. We measured resolved H₂ line profiles of 23 targets with inclination angles $> 15^\circ$ and found that these line profiles are reasonably well fitted by a single Gaussian component at or near the stellar radial velocity. Assuming a disk origin for these targets, we used the line widths to constrain the spatial distribution of the emitting molecules to $a \lesssim 3$ AU in most cases.
5. The inner radii of H₂ disks are roughly consistent with those of CO disks (measured from $\lambda \sim 5 \mu\text{m}$ spectroscopy).
6. Strong H₂ emission is observed at $a \gtrsim 0.2$ AU in a subsample of transitional disks ($n_{13-31} > 0.5$).

We thank Tom Ayres for custom processing of the STIS observations and the DAO of Tau team for enjoyable discussions during the course of this work. K.F. thanks Phil Armitage for helpful discussion regarding gas giant migration. We acknowledge the technical efforts of Nico Nell and David Morris, and E.S. and K.F. thank Brian Wood for input on Ly α profile reconstruction. R.D.A. acknowledges support from the Science & Technology Facilities Council (STFC) through an Advanced Fellowship (ST/G00711X/1). This work was supported by NASA

grants NNX08AC146 and NAS5-98043 to the University of Colorado at Boulder (*HST* programs 11533 and 12036) and made use of data from *HST* GO programs 8041, 11616, 11828, and 12361.

REFERENCES

- Akeson, R. L., Ciardi, D. R., van Belle, G. T., & Creech-Eakman, M. J. 2002, *ApJ*, **566**, 1124
- Alencar, S. H. P., Melo, C. H. F., Dullemond, C. P., et al. 2003, *A&A*, **409**, 1037
- Alexander, R. D., Clarke, C. J., & Pringle, J. E. 2006, *MNRAS*, **369**, 229
- Andrews, S. M., & Williams, J. P. 2007, *ApJ*, **659**, 705
- Andrews, S. M., Wilner, D. J., Espaillat, C., et al. 2011, *ApJ*, **732**, 42
- Ardila, D. R., Basri, G., Walter, F. M., Valenti, J. A., & Johns-Krull, C. M. 2002, *ApJ*, **566**, 1100
- Armitage, P. J. 2007, *ApJ*, **665**, 1381
- Armitage, P. J., Clarke, C. J., & Palla, F. 2003, *MNRAS*, **342**, 1139
- Armitage, P. J., Livio, M., Lubow, S. H., & Pringle, J. E. 2002, *MNRAS*, **334**, 248
- Ayres, T. R. 2010, *ApJS*, **187**, 149
- Bary, J. S., Weintraub, D. A., & Kastner, J. H. 2003, *ApJ*, **586**, 1136
- Bary, J. S., Weintraub, D. A., Shukla, S. J., Leisenring, J. M., & Kastner, J. H. 2008, *ApJ*, **678**, 1088
- Bast, J., Brown, J., Herczeg, G., van Dishoek, E., & Pontoppidan, K. 2011, *A&A*, **1**, 0
- Beck, T. L., McGregor, P. J., Takami, M., & Pyo, T.-S. 2008, *ApJ*, **676**, 472
- Bertout, C., Siess, L., & Cabrit, S. 2007, *A&A*, **473**, L21
- Bethell, T. J., & Bergin, E. A. 2011, *ApJ*, **739**, 78
- Brittain, S. D., Najita, J. R., & Carr, J. S. 2009, *ApJ*, **702**, 85
- Calvet, N., D'Alessio, P., Hartmann, L., et al. 2002, *ApJ*, **568**, 1008
- Calvet, N., D'Alessio, P., Watson, D. M., et al. 2005, *ApJ*, **630**, L185
- Calvet, N., & Gullbring, E. 1998, *ApJ*, **509**, 802
- Carmona, A., van den Ancker, M. E., Henning, T., et al. 2007, *A&A*, **476**, 853
- Carmona, A., van den Ancker, M. E., Henning, T., et al. 2008, *A&A*, **477**, 839
- Carr, J. S., & Najita, J. R. 2008, *Science*, **319**, 1504
- Carr, J. S., & Najita, J. R. 2011, *ApJ*, **733**, 102
- Chiang, E., & Murray-Clay, R. 2007, *Nature Phys.*, **3**, 604
- Coffey, D., Bacciotti, F., Woitas, J., Ray, T. P., & Eisloffel, J. 2004, *ApJ*, **604**, 758
- Comerón, F., & Fernández, M. 2010, *A&A*, **511**, A10
- Comerón, F., Fernández, M., Baraffe, I., Neuhäuser, R., & Kaas, A. A. 2003, *A&A*, **406**, 1001
- Danforth, C. W., Keeney, B. A., Stocke, J. T., Shull, J. M., & Yao, Y. 2010, *ApJ*, **720**, 976
- Dodson-Robinson, S. E., & Salyk, C. 2011, *ApJ*, **738**, 131
- Eisner, J. A., Hillenbrand, L. A., White, R. J., et al. 2007, *ApJ*, **669**, 1072
- Elias, J. H. 1978, *ApJ*, **224**, 857
- Espaillat, C., Calvet, N., D'Alessio, P., et al. 2007a, *ApJ*, **664**, L111
- Espaillat, C., Calvet, N., D'Alessio, P., et al. 2007b, *ApJ*, **670**, L135
- Espaillat, C., D'Alessio, P., Hernández, J., et al. 2010, *ApJ*, **717**, 441
- Espaillat, C., Furlan, E., D'Alessio, P., et al. 2011, *ApJ*, **728**, 49
- Evans, N. J., II, Dunham, M. M., Jørgensen, J. K., et al. 2009, *ApJS*, **181**, 321
- Fang, M., van Boekel, R., Wang, W., et al. 2009, *A&A*, **504**, 461
- Fedele, D., van den Ancker, M. E., Henning, T., Jayawardhana, R., & Oliveira, J. M. 2010, *A&A*, **510**, A72
- Feigelson, E. D., Lawson, W. A., & Garmire, G. P. 2003, *ApJ*, **599**, 1207
- Fogel, J. K. J., Bethell, T. J., Bergin, E. A., Calvet, N., & Semenov, D. 2011, *ApJ*, **726**, 29
- France, K., Burgh, E. B., Herczeg, G. J., et al. 2012, *ApJ*, **744**, 22
- France, K., Linsky, J. L., Brown, A., Froning, C. S., & Béland, S. 2010, *ApJ*, **715**, 596
- France, K., Schindhelm, E., Burgh, E. B., et al. 2011a, *ApJ*, **734**, 31
- France, K., Yang, H., & Linsky, J. L. 2011b, *ApJ*, **729**, 7
- Furlan, E., Hartmann, L., Calvet, N., et al. 2006, *ApJS*, **165**, 568
- Furlan, E., Watson, D. M., McClure, M. K., et al. 2009, *ApJ*, **703**, 1964
- Gahm, G. F., Walter, F. M., Stempels, H. C., Petrov, P. P., & Herczeg, G. J. 2008, *A&A*, **482**, L35
- García Lopez, R., Natta, A., Testi, L., & Habart, E. 2006, *A&A*, **459**, 837
- Gómez de Castro, A. I. 2009, *ApJ*, **698**, L108
- Gorti, U., Dullemond, C. P., & Hollenbach, D. 2009, *ApJ*, **705**, 1237
- Grady, C. A., Woodgate, B., Torres, C. A. O., et al. 2004, *ApJ*, **608**, 809
- Green, J. C., Froning, C. S., Osterman, S., et al. 2012, *ApJ*, **744**, 60
- Guenther, E. W., Esposito, M., Mundt, R., et al. 2007, *A&A*, **467**, 1147
- Gullbring, E., Calvet, N., Muzerolle, J., & Hartmann, L. 2000, *ApJ*, **544**, 927
- Gullbring, E., Hartmann, L., Briceno, C., & Calvet, N. 1998, *ApJ*, **492**, 323
- Günther, H. M., & Schmitt, J. H. M. M. 2008, *A&A*, **481**, 735

- Haisch, K. E., Jr., Lada, E. A., & Lada, C. J. 2001, *ApJ*, **553**, L153
- Hartigan, P., & Hillenbrand, L. 2009, *ApJ*, **705**, 1388
- Hartmann, L., Calvet, N., Gullbring, E., & D'Alessio, P. 1998, *ApJ*, **495**, 385
- Hartmann, L., Hewett, R., Stahler, S., & Mathieu, R. D. 1986, *ApJ*, **309**, 275
- Hayashi, C., Nakazawa, K., & Nakagawa, Y. 1985, in *Protostars and Planets II* (A86-12626 03-90), ed. D. C. Black & M. S. Matthews (Tucson, AZ: Univ. Arizona Press), 1100
- Herczeg, G. J., & Hillenbrand, L. A. 2008, *ApJ*, **681**, 594
- Herczeg, G. J., Linsky, J. L., Valenti, J. A., Johns-Krull, C. M., & Wood, B. E. 2002, *ApJ*, **572**, 310
- Herczeg, G. J., Linsky, J. L., Walter, F. M., Gahm, G. F., & Johns-Krull, C. M. 2006, *ApJS*, **165**, 256
- Herczeg, G. J., Najita, J. R., Hillenbrand, L. A., & Pascucci, I. 2007, *ApJ*, **670**, 509
- Herczeg, G. J., Walter, F. M., Linsky, J. L., et al. 2005, *AJ*, **129**, 2777
- Herczeg, G. J., Wood, B. E., Linsky, J. L., Valenti, J. A., & Johns-Krull, C. M. 2004, *ApJ*, **607**, 369
- Hernández, J., Hartmann, L., Megeath, T., et al. 2007, *ApJ*, **662**, 1067
- Hirth, G. A., Mundt, R., Solf, J., & Ray, T. P. 1994, *ApJ*, **427**, L99
- Hussain, G. A. J., Collier Cameron, A., Jardine, M. M., et al. 2009, *MNRAS*, **398**, 189
- Ida, S., & Lin, D. N. C. 2004, *ApJ*, **604**, 388
- Ingleby, L., Calvet, N., Bergin, E., et al. 2009, *ApJ*, **703**, L137
- Ingleby, L., Calvet, N., Bergin, E., et al. 2011a, *ApJ*, **743**, 1051
- Ingleby, L., Calvet, N., Hernández, J., et al. 2011b, *AJ*, **141**, 127
- Itoh, Y., Sugitani, K., Ogura, K., & Tamura, M. 2003, *PASJ*, **55**, L77
- Jensen, E. L. N., & Mathieu, R. D. 1997, *AJ*, **114**, 301
- Johns-Krull, C. M., & Valenti, J. A. 2001, *ApJ*, **561**, 1060
- Johns-Krull, C. M., Valenti, J. A., & Linsky, J. L. 2000, *ApJ*, **539**, 815
- Kenyon, S. J., & Hartmann, L. 1995, *ApJS*, **101**, 117
- Kim, K. H., Watson, D. M., Manoj, P., et al. 2009, *ApJ*, **700**, 1017
- Kraus, A. L., & Hillenbrand, L. A. 2009, *ApJ*, **704**, 531
- Kraus, A. L., Ireland, M. J., Hillenbrand, L. A., & Martinache, F. 2012, *ApJ*, **745**, 19
- Kriss, G. A. 2011, Improved Medium Resolution Line Spread Functions for COS FUV Spectra, Technical Report
- Lawson, W. A., Crause, L. A., Mamajek, E. E., & Feigelson, E. D. 2001, *MNRAS*, **321**, 57
- Lawson, W. A., Feigelson, E. D., & Huenemoerder, D. P. 1996, *MNRAS*, **280**, 1071
- Lawson, W. A., Lyo, A., & Muzerolle, J. 2004, *MNRAS*, **351**, L39
- Lepp, S., & Shull, J. M. 1983, *ApJ*, **270**, 578
- Loinard, L., Torres, R. M., Mioduszewski, A. J., et al. 2007, *ApJ*, **671**, 546
- Luhman, K. L. 2004, *ApJ*, **602**, 816
- Luhman, K. L., Allen, P. R., Espaillat, C., Hartmann, L., & Calvet, N. 2010, *ApJS*, **186**, 111
- Mamajek, E. E., Lawson, W. A., & Feigelson, E. D. 1999, *ApJ*, **516**, L77
- Markwardt, C. B. 2009, in *ASP Conf. Ser. 411, Astronomical Data Analysis Software and Systems XVIII*, ed. D. A. Bohlender, D. Durand, & P. Dowler (San Francisco, CA: ASP), 251
- Melnikov, S. Y., Eisloffel, J., Bacciotti, F., Woitas, J., & Ray, T. P. 2009, *A&A*, **506**, 763
- Merín, B., Brown, J. M., Oliveira, I., et al. 2010, *ApJ*, **718**, 1200
- Muzerolle, J., Calvet, N., Hartmann, L., & D'Alessio, P. 2003, *ApJ*, **597**, L149
- Najita, J., Carr, J. S., & Mathieu, R. D. 2003, *ApJ*, **589**, 931
- Najita, J. R., Crockett, N., & Carr, J. S. 2008, *ApJ*, **687**, 1168
- Najita, J. R., Doppmann, G. W., Bitner, M. A., et al. 2009, *ApJ*, **697**, 957
- Najita, J. R., Strom, S. E., & Muzerolle, J. 2007, *MNRAS*, **378**, 369
- Neuhäuser, R., Brandner, W., Eckart, A., et al. 2000, *A&A*, **354**, L9
- Nomura, H., Aikawa, Y., Tsujimoto, M., Nakagawa, Y., & Millar, T. J. 2007, *ApJ*, **661**, 334
- Ostern, S., Green, J., Froning, C., et al. 2011, *Ap&SS*, **335**, 257
- Pascucci, I., Gorti, U., Hollenbach, D., et al. 2006, *ApJ*, **651**, 1177
- Pascucci, I., Hollenbach, D., Najita, J., et al. 2007, *ApJ*, **663**, 383
- Pascucci, I., Sterzik, M., Alexander, R. D., et al. 2011, *ApJ*, **736**, 13
- Plavchan, P., Werner, M. W., Chen, C. H., et al. 2009, *ApJ*, **698**, 1068
- Pontoppidan, K. M., Blake, G. A., & Smette, A. 2011, *ApJ*, **733**, 84
- Pontoppidan, K. M., Blake, G. A., van Dishoeck, E. F., et al. 2008, *ApJ*, **684**, 1323
- Quast, G. R., Torres, C. A. O., de La Reza, R., da Silva, L., & Mayor, M. 2000, in *IAU Symp. 200, Birth and Evolution of Binary Stars*, ed. B. Reipurth & H. Zinnecker (Cambridge: Cambridge Univ. Press), 28P
- Ramsay Howat, S. K., & Greaves, J. S. 2007, *MNRAS*, **379**, 1658
- Ricci, L., Testi, L., Natta, A., et al. 2010, *A&A*, **512**, A15
- Rice, W. K. M., Wood, K., Armitage, P. J., Whitney, B. A., & Bjorkman, J. E. 2003, *MNRAS*, **342**, 79
- Rodriguez, D. R., Kastner, J. H., Wilner, D., & Qi, C. 2010, *ApJ*, **720**, 1684
- Sacco, G. G., Flaccomio, E., Pascucci, I., et al. 2012, *ApJ*, **747**, 142
- Salyk, C., Blake, G. A., Boogert, A. C. A., & Brown, J. M. 2009, *ApJ*, **699**, 330
- Salyk, C., Blake, G. A., Boogert, A. C. A., & Brown, J. M. 2011a, *ApJ*, **743**, 112
- Salyk, C., Pontoppidan, K. M., Blake, G. A., Najita, J. R., & Carr, J. S. 2011b, *ApJ*, **731**, 130
- Salyk, C., Pontoppidan, K. M., Blake, G. A., et al. 2008, *ApJ*, **676**, L49
- Saucedo, J., Calvet, N., Hartmann, L., & Raymond, J. 2003, *ApJ*, **591**, 275
- Schindhelm, E., France, K., Burgh, E. B., et al. 2012a, *ApJ*, **746**, 97
- Schindhelm, E., France, K., Herczeg, G., & Bergin, E. 2012b, *ApJ*, submitted
- Shull, J. M. 1978, *ApJ*, **224**, 841
- Sicilia-Aguilar, A., Henning, T., & Hartmann, L. W. 2010, *ApJ*, **710**, 597
- Siess, L., Dufour, E., & Forestini, M. 2000, *A&A*, **358**, 593
- Simon, M., Dutrey, A., & Guilloteau, S. 2000, *ApJ*, **545**, 1034
- Stempels, H. C., Gahm, G. F., & Petrov, P. P. 2007, *A&A*, **461**, 253
- Strom, K. M., Strom, S. E., Edwards, S., Cabrit, S., & Skrutskie, M. F. 1989, *AJ*, **97**, 1451
- Takami, M., Bailey, J., Gledhill, T. M., Chrysostomou, A., & Hough, J. H. 2001, *MNRAS*, **323**, 177
- Trilling, D. E., Lunine, J. I., & Benz, W. 2002, *A&A*, **394**, 241
- Valenti, J. A., Johns-Krull, C. M., & Linsky, J. L. 2000, *ApJS*, **129**, 399
- van Boekel, R., Min, M., Waters, L. B. F. M., et al. 2005, *A&A*, **437**, 189
- van Leeuwen, F. 2007, *A&A*, **474**, 653
- Walter, F. M., Herczeg, G., Brown, A., et al. 2003, *AJ*, **126**, 3076
- Ward, W. R. 1997, *Icarus*, **126**, 261
- Webb, R. A., Zuckerman, B., Platais, I., et al. 1999, *ApJ*, **512**, L63
- White, R. J., & Ghez, A. M. 2001, *ApJ*, **556**, 265
- Williams, J. P., & Cieza, L. A. 2011, *ARA&A*, **49**, 67
- Woitas, J., Ray, T. P., Bacciotti, F., Davis, C. J., & Eisloffel, J. 2002, *ApJ*, **580**, 336
- Wood, B. E., & Karovska, M. 2004, *ApJ*, **601**, 502
- Wood, B. E., Karovska, M., & Raymond, J. C. 2002, *ApJ*, **575**, 1057
- Wyatt, M. C. 2008, *ARA&A*, **46**, 339
- Yang, H., Herczeg, G. J., Linsky, J. L., et al. 2012, *ApJ*, **744**, 121
- Yang, H., Linsky, J., & France, K. 2011, *ApJ*, **0**, L1